



# In Situ Transmission Electron Microscopy Investigation of Dislocation Interactions

# 6

Josh Kacher, Ben P. Eftink, and Ian M. Robertson

## Contents

1	Introduction .....	132
2	Dislocation Nucleation, Propagation, and Multiplication .....	133
2.1	Dislocation Nucleation .....	133
2.2	Dislocation Propagation .....	136
2.3	Dislocation Multiplication .....	138
3	Dislocation Interactions with Defect Fields .....	140
3.1	Solid Solution Atoms .....	141
3.2	Oxide Dispersion Strengthened Materials .....	142
3.3	Irradiation-Induced Defects .....	145
4	Dislocation Interactions with Isolated Obstacles .....	146
4.1	Dislocation Loops .....	146
4.2	Stacking Fault Tetrahedra .....	147
4.3	Precipitates .....	150
5	Dislocation–Grain Boundary Interactions .....	150
5.1	General Characteristics .....	152
5.2	Temperature Effects .....	153
5.3	Coherent Twin Boundaries .....	155
5.4	Propagation Limited Systems: Irradiated Materials .....	158
5.5	Confined Microstructure: Ultrafine Grained and Nanotwinned Materials .....	161
6	Conclusion .....	163
	References .....	164

---

J. Kacher (✉)

Georgia Institute of Technology, Materials Science and Engineering, Atlanta, GA, USA

e-mail: [josh.kacher@mse.gatech.edu](mailto:josh.kacher@mse.gatech.edu)

B. P. Eftink

Los Alamos National Laboratory, MST-8 Materials Science in Radiation and Dynamic Extremes,  
Los Alamos, NM, USA

I. M. Robertson

University of Wisconsin-Madison, Materials Science and Engineering, Madison, WI, USA

e-mail: [enr-dean@enr.wisc.edu](mailto:enr-dean@enr.wisc.edu)

---

**Abstract**

This chapter provides a broad overview of dislocation interactions investigated via in situ transmission electron microscopy (TEM) deformation experiments. The discussion of these interactions is divided according to the interaction of interest, with the first section exploring the mechanics and energetics governing dislocation nucleation, propagation, and multiplication. The following two sections investigate dislocation interactions with isolated defects and defect fields, including interactions involving irradiation-induced defects, solute atoms, and second-phase particles. The final section discusses dislocation–grain boundary interactions with a focus on understanding how the local grain boundary structure and surrounding microstructure dictate the dislocation transfer process. Two unique advantages of TEM imaging for dislocation interactions will be highlighted throughout this chapter: the ability to capture dislocation interactions at sufficient spatial and temporal resolution to resolve complex interactions, and the ability to resolve salient features of the dislocation interactions using diffraction contrast imaging. This second advantage is used to characterize structural and geometrical factors influencing dislocation interactions, including the dislocation Burgers vector, line direction, and slip plane, crystallographic orientation, and boundary habitat planes.

---

**Keywords**

Transmission electron microscopy · In situ deformation · Dislocations · Plasticity · Strengthening mechanisms

---

## 1 Introduction

The mechanical properties of metals are largely dictated by the activity of dislocations, including their generation, propagation, and interaction with other defects such as precipitates and grain boundaries. Transmission electron microscopy (TEM) is uniquely capable of resolving complex dislocation interactions in real time and at sufficient resolution to capture the unit processes dictating an interaction. In addition, using diffraction-contrast analysis, relevant dislocation parameters such as Burgers vector, slip plane, and line direction can be characterized and applied to understand dislocation processes. This chapter will review in situ TEM-based experiments devoted to understanding the following dislocation interactions:

1. Dislocation nucleation, propagation, and multiplication
2. Dislocation interactions with defect fields
3. Dislocation interactions with isolated obstacles
4. Dislocation–grain boundary interactions

Although defects play a role in the deformation of ceramics and polymers, this chapter will focus primarily on dislocation interactions in metals.

## 2 Dislocation Nucleation, Propagation, and Multiplication

One of the original successes of electron microscopy characterization was proving the existence of dislocations [1]. Since that time, many studies have been published seeking to characterize the most fundamental aspects of dislocation behavior. These studies have two broad objectives: understanding the mechanisms by which dislocations operate and calculating the various energies/energy barriers associated with dislocation activity. This section will review studies performed to understand dislocation nucleation, multiplication, and propagation in a variety of systems.

### 2.1 Dislocation Nucleation

The original impetus for proposing the existence of dislocations was to explain the discrepancy between the theoretical strength of a material, or the strength needed to shear the atomic bonds in a material, and the observed strength. It is now understood that the strength of a material is related to the resolved shear stress needed to propagate dislocations through the matrix. However, a notable exception is in the case of dislocation free materials in which there are no preexisting dislocations for stresses to act on. In these materials, the theoretical strength and measured strength converge. This behavior was first observed in dislocation-free Sn whiskers [2], and, with the prevalence of nanomaterials, is becoming increasingly applicable. This emergence of nanomaterials, as well as advances in sample fabrication and nanoscale testing technologies, has motivated a number of studies into the nucleation mechanisms and energy of dislocations in initially dislocation-free materials.

Due to the imposing energy barrier against homogeneous nucleation, the vast majority of dislocation nucleation occurs at preexisting defects, including interfaces. Understanding the energy barriers to dislocation nucleation is important in modeling the strength of nanoscale materials in which the initial defect population is often near zero. Surface dislocation nucleation has been explored under both tension [3–5] and compression [6, 7] using quantitative in situ TEM indentation holders. These holders record the load and displacement while the sample is deformed via direct indentation or in tension using a push-to-pull device.

Lu et al. investigated surface dislocation nucleation in ultrathin (7–10 nm diameter) gold wires [4]. Using an atomic force microscopy (AFM) tip inside the TEM, they conducted tensile tests while imaging the sample in high resolution. They found that, upon the onset of plasticity, the stress dropped precipitously. High resolution imaging coupled with fast Fourier transforms of the atomic resolution images showed that necking of the sample occurred along  $\{111\}$  slip bands, suggesting that dislocation propagation was responsible for the observed deformation (Fig. 1). The first instance of dislocation activity in this test, as suggested by morphological changes of the nanowire, is indicated by the arrow in Fig. 1c. With increasing strain, an adjacent dislocation system activated, contributing to the necking of the wire. Dislocation activity and necking continued until final fracture occurred. Although

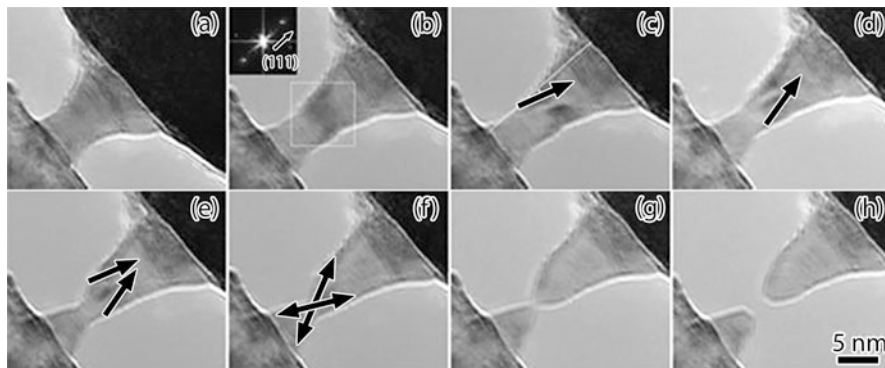


**Fig. 1** HRTEM images of a short gold nanowire under tensile testing (a)–(h): After the elastic deformation region (a)–(b), initial surface dislocation nucleation is indicated by the arrow in (c). Arrows in (d)–(f) indicate more similar dislocations emitted from both sides of the nanowire surfaces, and a neck (e)–(g) was formed in the middle section of the nanowire until the final fracture occurred as shown in (h). The insert in (b) shows a fast Fourier transform image calculated from the image inside the white square, showing the wire orientation (Image reused with permission of Springer from [4])

the strength of the nanowires was calculated, the authors did not relate this to the dislocation nucleation stress.

Chen et al. studied the effects of temperature and strain rate on the surface nucleation of dislocations in dislocation-free Pd nanowhiskers under uniaxial tensile loads using a picoindenter holder combined with a push-to-pull device [3] (Fig. 2a). Multiple samples were tested in situ in the TEM while systematically varying the applied strain rate and test temperature. They found that the samples could experience significant stresses, in the GPa regime, with no dislocation nucleation. That is, the samples underwent true elastic deformation. At a sufficiently high stress level, TEM imaging revealed that the plastic deformation was accommodated by the nucleation of surface dislocations or twins (Fig. 2f–i). Varying the strain rate was not found to influence the dislocation nucleation strength. Temperature variations, in contrast, strongly influenced nucleation strength, with the sample yield strength decreasing from 5.8 to 2.8 GPa with a temperature increase from 93 to 447 K. This temperature correlation is significantly stronger than the strength–temperature correlation found in bulk materials, suggesting that the barrier strength to dislocation nucleation is much more temperature dependent than the barrier to propagation of preexisting dislocations or the nucleation of dislocations from grain boundaries. Chen et al. attributed this temperature dependence to a thermally active surface diffusion mechanism for dislocation nucleation.

In contrast to Chen et al., who used indirect measures to calculate the dislocation nucleation stress, Li et al. directly quantified the stress needed to nucleate dislocations using measured atomic displacements during in situ TEM deformation coupled with first principles calculations [6]. They indented a TiN thin film along two different crystallographic directions, the  $\langle 111 \rangle$  and  $\langle 100 \rangle$ , to selectively activate

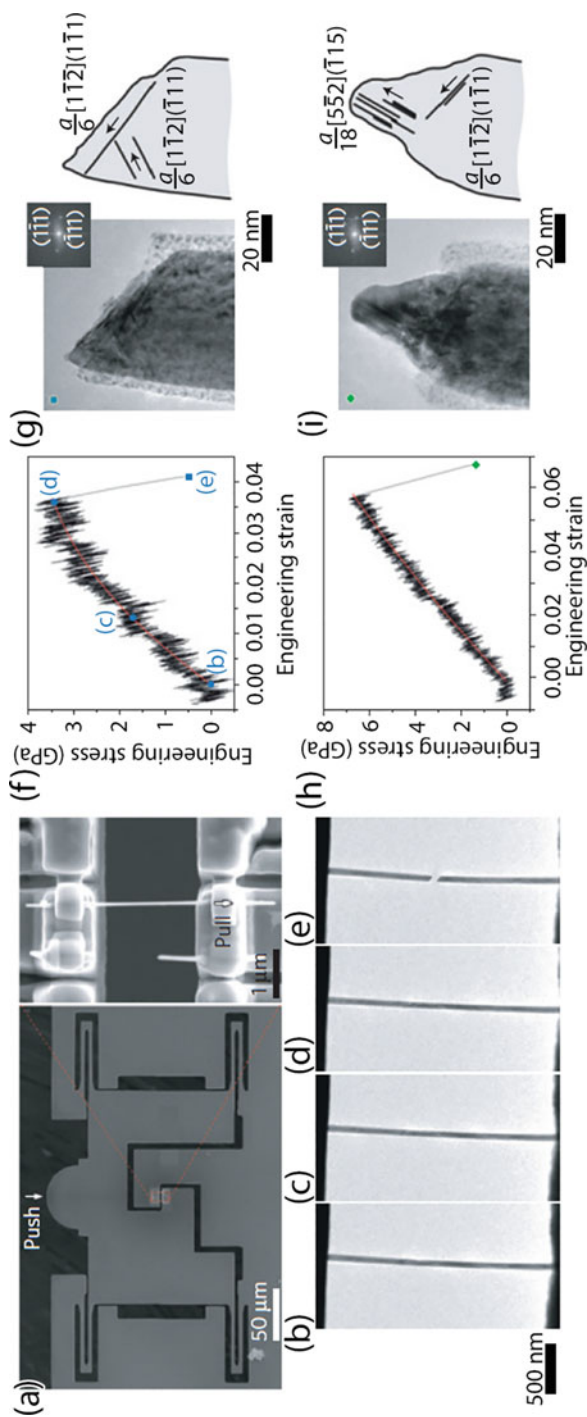


**Fig. 2** (a) Image of push-to-pull device with enlarged view showing mounted nanowires. (b–e) Image sequence of nanowire during in situ straining experiment. (f) Stress/strain curve associated with image sequence. (g) Fracture surface of nanowire after test with diffraction pattern showing fracture planes and active dislocation systems. (h–i) Stress strain curve and fracture surface of nanowire test conducted under similar conditions. Both tests were conducted at room temperature. Reprinted by permission from Macmillan Publishers Ltd: Nature Materials (3) copyright 2015

the  $\{111\}\langle 110\rangle$  and  $\{110\}\langle 110\rangle$  slip systems, respectively. While indenting along a  $\langle 111\rangle$  direction, they observed the emission of a partial dislocation from the region beneath the indenter tip. High resolution imaging showed that the dislocation resided on the  $(1\bar{1}1)$  plane with Burgers vector  $a_0/6[\bar{1}12]$  and line direction parallel to  $[110]$ . With continued compression, the trailing partial dislocation was also emitted and recombined with the lead partial dislocation, resulting in the atomic lattice being restored to its original state. The character of the trailing partial dislocation was not reported. In order to quantify the dislocation nucleation stress, the lattice strain was calculated by measuring the atomic displacements from the perfect lattice configuration near the indenter tip 0.3 s prior to the emission of the lead partial dislocation. Density functional theory (DFT) calculations were used to determine the nonlinear elastic behavior at high stresses. The critical nucleation stress was measured as 13.8 GPa. Repeating the experiment with a loading direction parallel to  $\langle 100\rangle$ , they observed the emission of a perfect edge dislocation on a  $\{011\}$  plane. The critical stress in this second experiment was calculated as 6.7 GPa. The difference in the measured critical stresses was attributed to dislocations in the  $\{111\}\langle 110\rangle$  systems experiencing a larger Peierls stress.

## 2.2 Dislocation Propagation

Dislocation propagation occurs via glide, cross-slip, and climb. Dislocation motion and the energetics dictating their motion is central to understanding and modelling the flow stress of materials. In FCC systems, dislocation motion is limited almost exclusively to close packed planes and directions. In lower symmetry crystals such as HCP, the lack of available slip systems often forces the activation of less energetically favorable systems. The behavior of these dislocations and mechanisms that dictate their behavior has been studied extensively by in situ TEM deformation experiments [8–13]. Here we focus on propagation of dislocations in HCP materials.

In most HCP materials, dislocation activity is dominated by propagation of **a**-type dislocations gliding on either the basal plane or the prismatic plane, with the energetically more favorable plane generally determined by the  $c/a$  ratio of the crystal lattice. Due to the restricted number of available slip systems, HCP systems tend to be significantly less ductile than FCC materials, with twin activation serving as an additional deformation mechanism. As dislocation glide on the different available slip planes varies energetically, deformation of HCP materials has a strong thermal component. For example, Couret and Caillard investigated the behavior of prismatic dislocation systems in Mg over a temperature range from 50 to 673 K [11, 12]. Crystal directions were carefully aligned with the tensile axis such that dislocation activity on the basal plane, the energetically favorable plane in Mg, was suppressed and prismatic glide was activated. They observed that dislocation motion was strongly anisotropic, with edge components of dislocations gliding easily at low temperatures but screw components requiring significantly higher stress levels to operate. This behavior was strongly dependent on the temperature. At 50 K, no

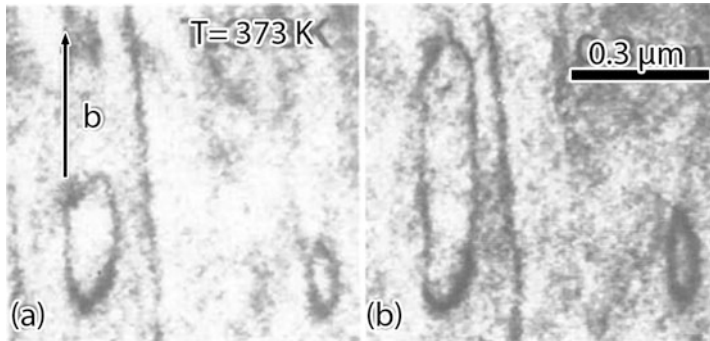


**Fig. 3** Dislocation loop expansion at 373 K in Mg during in situ TEM deformation showing asymmetric glide of edge and screw components (Image modified with permission from [11])

screw dislocation activity was observed, though limited motion of edge dislocations continued. As the temperature increased, the screw components increased in activity and the anisotropy between the screw and edge dislocation mobilities decreased (see, for example, dislocation glide at 373 K in Fig. 3). At the peak temperature,  $\sim 673$  K, climb mechanisms activated and the dislocations formed sub-boundaries. At all temperatures, dislocation propagation proceeded via cross-slip between the basal and prismatic planes.

Investigations of the tension/compression behavior of certain HCP alloys such as Ti have shown a marked asymmetry in the mechanical properties. This asymmetry has been tied to the dislocation core structure, which can have a strong influence on the dislocation propagation behavior [14]. Clouet et al. investigated this behavior in two different systems, Ti and Zr [10]. Video frames of the dislocation motion taken during in situ TEM deformation and difference images showing the dislocation motion between frames are shown in Fig. 4. Despite their similar electronic structures, dislocation motion in the two materials was seen to proceed in very different manners. In both systems, the dominant slip plane is the prismatic plane. However, while dislocations in Zr propagated smoothly, the motion of dislocations in Ti was jerky and intermittent. Intermittent flow of dislocations in  $\alpha$ -Ti was also observed by Kacher and Robertson, who noted that this behavior led to dislocation generation via cross-slip mechanisms [15]. Clouet et al. traced the different behaviors to the core structure of the dislocations. In both systems, the dislocation core spreads on the pyramidal and first order prismatic planes. In Zr, the stable plane is the prismatic plane, which corresponds to the lowest energy glide plane. In Ti, the prismatic plane is the lowest energy glide plane, but core spreading onto the pyramidal plane is more stable. As a result, the dislocations in Zr exhibit easy glide during deformation while dislocations in Ti display frequent cross-slip events onto the pyramidal plane, creating sessile jogs during the deformation process. They hypothesized that this behavior could be influenced by the solute state of the material, suggesting a pathway to understanding the strengthening effects of impurities such as O in Ti.



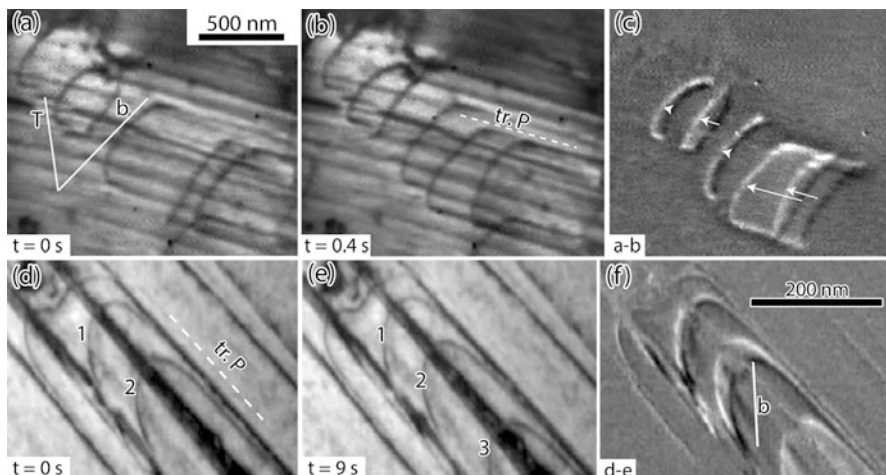


**Fig. 4** (a–c) Dislocation glide in  $\alpha$ -Ti during in situ TEM deformation. Difference image shown in (c). Slope and line direction shown in (a) and plane trace is shown in (b). (d–f) Dislocation glide in Zr during in situ TEM deformation. Difference image shown in (f). Slip plane trace indicated in (d) and Burgers vector in (f) (Reprinted by permission from Macmillan Publishers Ltd.: Nature Materials [10] copyright 2015)

### 2.3 Dislocation Multiplication

The two primary dislocation-based mechanisms for dislocation multiplication (excluding boundary and interface sources) are the activation of Frank-Read sources and via double cross-slip events. As both of these mechanisms involve the expansion of dislocation loops, their operation can be significantly influenced by the thin film geometry needed for TEM analysis. For example, although Frank-Read sources are expected to be a common mechanism for dislocation multiplication, observations made during in situ TEM deformation are limited almost exclusively to single-arm sources.

One way the effects of free surfaces have been partly alleviated in in situ TEM investigations is by using high-voltage electron microscopes (HVEM) in which voltages range from 1 to 3 MV and sample thicknesses can extend into the  $\mu\text{m}$  range. Appel et al. investigated dislocation motion under tensile deformation in 1  $\mu\text{m}$  thick MgO films [16]. Video frames of the interaction are shown in Fig. 5. They observed that gliding screw dislocations formed large jogged sections as they propagated through the matrix (Fig. 5a–c). As these jogged sections were sessile, they trailed the propagating dislocation front (Fig. 5d–e). The connecting segments, which were edge in nature, continued to elongate as the screw segment propagated, eventually pinching off and remaining in the matrix as dislocation debris (Fig. 5e–f).

Similar experiments have been conducted in a range of materials, though mostly in oxides or ceramics where the electron beam damage effects are less pronounced. Werner et al. investigated dislocation motion in Si during high temperature straining [17]. They observed a mechanism for dislocation source formation where a screw dislocation and mixed-character dislocation with parallel Burgers vectors but propagating on different



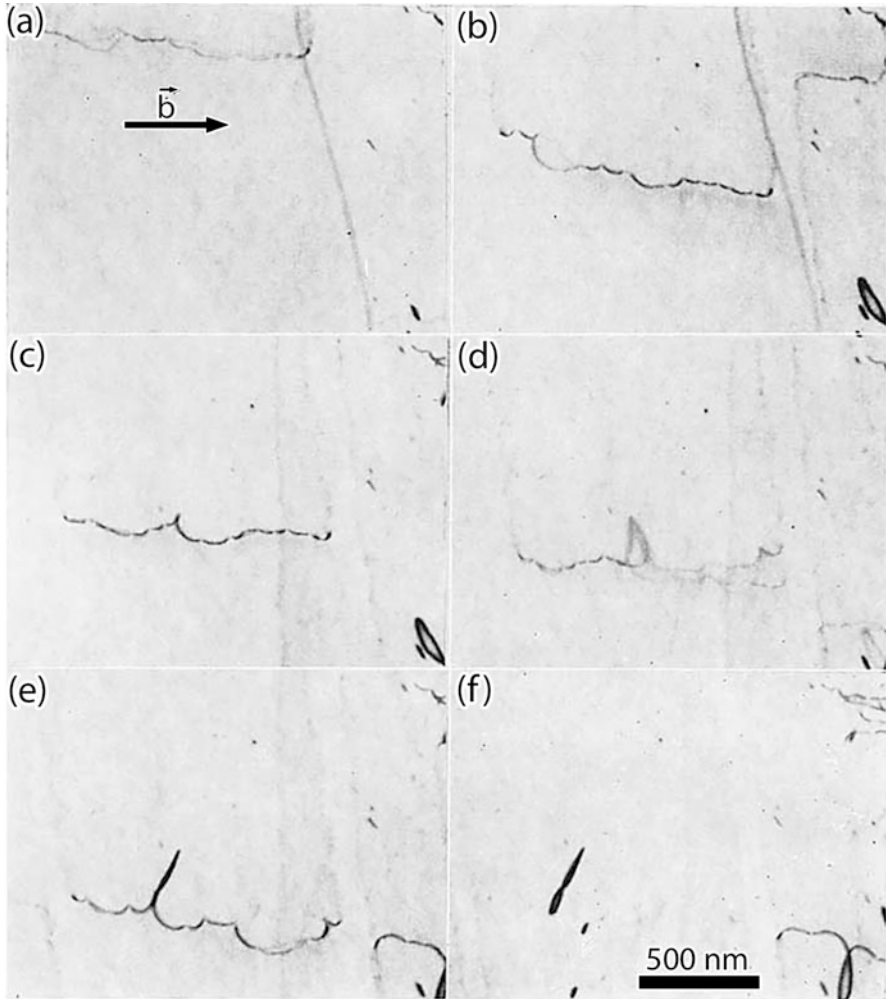


**Fig. 5** Image sequence showing an edge dislocation dipole forming behind gliding screw dislocation during in situ TEM deformation of a MgO film (Image used with permission from [16])

glide planes intersect and form a node. Once formed, the node acts as a pinning point for the operation of a single arm dislocation source. Baither et al. investigated high temperature deformation behavior of dislocations in cubic zirconia [18]. They found that the dislocation multiplication mechanisms were dependent on the crystallographic orientation in relation to the tensile axis and were strongly influenced by the free surface. Samples with a (110) foil surface facilitated easy escape of screw dislocations through the sample surface, restricting the number of super jogs forming from cross-slip events. As the super jogs were the primary source for dislocation multiplication, few sources were seen to operate. In contrast, samples with a  $(\bar{1}11)$  free surface, multiple  $\alpha$ -shaped

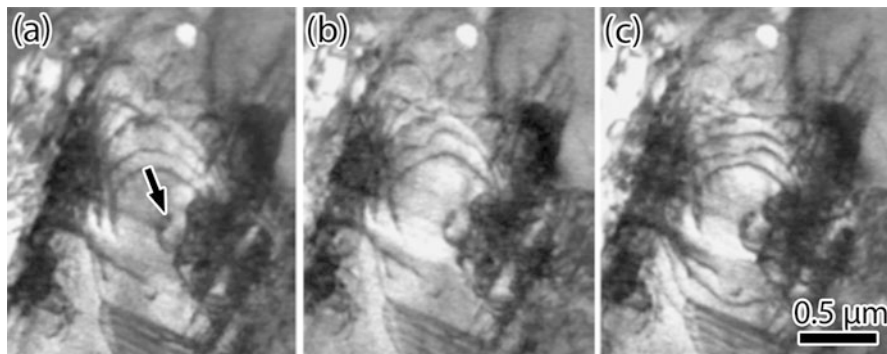


**Fig. 6** Dislocations generated from a single arm dislocation source in an austenite grain during in situ TEM deformation of a duplex steel. Frames (b) and (c) were captured 58 s and 126 s after (a), respectively. Arrow in (a) indicates location of dislocation source (Image used with permission from [19])

dislocation segments were found in the deformed samples. These dislocation configurations operated as dislocation sources, producing shear loops repeatedly during deformation.

Messerschmidt and Bartsch summarized many of these findings, focusing their remarks on the influence of the cross-slip behavior of the materials on dislocation multiplication mechanisms [19]. In materials where the cross-slip plane is equivalent to the primary glide plane, such as is found in FCC materials, the barrier to dislocation multiplication via cross-slip is relatively low. In many materials, especially those with lower symmetry, the flow stress for glide on the cross-slip plane is substantially higher than on the primary plane. This significantly decreases the cross-slip height, restricting the operation of cross-slip based dislocation multiplication mechanisms. Thus, dislocation generation via a Frank-Read source mechanism was found to be more prevalent in lower symmetry crystals. Messerschmidt and Bartsch also experimentally demonstrated the effects of back-stress in terminating dislocation sources. Figure 6 shows dislocation multiplication occurring at a single-arm dislocation source in an austenite grain in duplex steel. In the middle of the grain, a single-arm source is visible, identifiable by the helical shape indicated by an arrow. As the sample was deformed, dislocations were generated and propagated from the source, piling up at a nearby phase boundary. After the accumulation of several dislocations, the back stress became sufficient to shield the stresses operating on the source and terminate further dislocation multiplication. The source activity restarted once the dislocations transferred across the boundary and away from the source.

### 3 Dislocation Interactions with Defect Fields

Fields of defects in materials can be introduced to strengthen a material such as in the case of oxide dispersoids or solid solution interstitial and substitutional atoms. Dispersed defects can also be detrimental to the properties of materials such as in

the case of dislocation loops or stacking fault tetrahedra introduced during irradiation by energetic particles. The impact on mechanical properties, whether beneficial or detrimental, is directly related to how dislocations interact with the defects. In situ TEM characterization techniques are well suited to directly observe dislocation interactions with individual and fields of defects and have the temporal and spatial resolution necessary to determine the mechanisms associated with the interactions. While atomistic simulations provide a higher temporal and spatial resolution than experimental techniques, the simulations are limited in size- and time-scales.

### 3.1 Solid Solution Atoms

Solid solution strengthening is a common strengthening approach involving additions of interstitial or substitutional atoms to a material. Depending on the solute and concentration, mechanical properties may vary. For example, the addition of carbon increases the strength of Fe whereas the addition of hydrogen to most metals has a detrimental embrittling effect. The mechanisms proposed to account for these changes are attributed to their interaction with dislocations; particularly, how the stress field of dislocations interacts with the solutes.

In Fe, solute carbon atoms diffuse to and occupy the octahedral position in the BCC lattice. The resultant matrix strain fields interact with glissile dislocations and add resistance to their movement. This is believed to be the cause of dynamic strain aging and yield stress drop in Fe. The impact of carbon concentration on dislocation slip in Fe has not been directly observed until recently. Fe samples with carbon concentrations ranging from 1 to 230 ppm were subjected to in situ TEM deformation at temperatures ranging from 293 to 473 K [20]. The experiments confirmed the influence of temperature on dynamic strain aging and its effect on the bulk mechanical response of Fe. At room temperature, dislocation glide was smooth for both 1 and 16 ppm carbon samples, with the 230 ppm carbon sample exhibiting serrated dislocation flow. Higher temperatures, 373 K for 16 ppm carbon and 453 K for 1 ppm carbon, induced serrated dislocation flow at lower carbon concentrations. Higher temperatures increase the mobility of carbon and aids carbon diffusion to the dislocations. Carbon at the dislocations also had the effect of changing the character of the dislocations to screw dislocations.

In contrast to carbon in Fe, in situ TEM deformation experiments have found that hydrogen additions to most metals increase the dislocation mobility [21]. Shih et al. used an aperture-limited environmental cell TEM in combination with in situ deformation to investigate the influence of a hydrogen-environment on dislocation mobility [22]. By introducing the hydrogen environment in situ during deformation, the dislocation behavior with and without the influence of hydrogen could be directly compared. Shih et al. observed that the dislocation velocity increased from  $5 \times 10^{-2} \mu\text{m s}^{-1}$  in vacuum to an average  $7.6 \times 10^{-2} \mu\text{m s}^{-1}$  in 13 kPa of hydrogen. They hypothesized that this change in dislocation velocity was due to hydrogen decreasing the stress fields associated with the dislocations such that the interaction energy with other elastic obstacles was decreased – the so-called hydrogen-shielding

mechanism of hydrogen embrittlement [23]. Comparing the carbon and hydrogen additions to materials shows dislocation motion can be either inhibited or enhanced by solutes.

Substitutional atom replacement in Fe has been investigated by alloying controlled concentrations of Ni, Si, Cr, and Al [20]. Alloys were prepared such that the carbon content was constant at 16 ppm. For the case of Ni and Si, minimal effect was observed for dislocation motion, the only notable difference being the more frequent occurrence of superjog formation. This was thought to be due to cross-slip at substitutional atoms. Additions of Cr at 5 and 14 at% and Al at 17 wt% were observed to increase the onset temperature of dynamic strain aging as well as reduce the prevalence of screw character dislocations. This behavior was attributed to an attraction of the carbon atoms to Cr and Al atoms. Clusters of Mg in an Al–Mg alloy have also been observed to interact with and pin dislocations, resulting in the formation of dislocation debris during dislocation propagation [24]. Using electron energy loss spectroscopy (EELS) analysis, the authors found an increased Mg concentration surrounding dislocation loops formed during deformation, suggesting that Mg was preferentially inhabiting the dislocation core. These systematic studies on the influence of solute additions on dislocation behavior can act as guides in the development and application of new alloys.

### 3.2 Oxide Dispersion Strengthened Materials

Similar to solid solution atoms, oxide dispersions introduced in materials have the effect of inhibiting dislocation motion. Metals with oxide dispersions have been subject to interest for improved high temperature creep strength as well as irradiation tolerance. Studies have used in situ TEM deformation experiments to observe dislocation interactions with fine oxide precipitates at elevated temperatures and, to a limited extent, at room temperature [25–27]. Elevated temperature in situ deformation studies of several oxide dispersion strengthened (ODS) alloys have confirmed the mechanism for precipitate bypass is rate limited by the detachment process at the departure side of the precipitate [25–27]. This mechanism is consistent for several ODS alloys, including INCOLOY MA 956, INCONEL MA 754, NiAl, Ni<sub>3</sub>Al, and FeAl. At room temperature, particle shearing or Orowan bypass mechanisms are expected to be active.

The combination of in situ heating and straining TEM experiments allows the differences in deformation behavior across temperature ranges to be compared directly. When considering ODS alloys, the bypass mechanism of precipitates for dislocations has been found to change with temperature. An Fe–Cr, INCOLOY MA956, ODS alloy has been investigated using in situ TEM heating and deformation experiments to determine the dynamics of this process [25]. At room temperature, strengthening can be partially attributed to the Orowan precipitate bypass mechanism while at elevated temperatures the dislocations are able to climb to bypass the oxide dispersoids. During in situ straining at 700 °C, the authors grouped the bypass mechanism into four steps: (i) viscous slip until encountering a precipitate pinning

point, (ii) encountering a precipitate and quickly overcoming it by climb, (iii) pinning of the dislocation at the departure side of the precipitate as the dislocation bows out on both sides until reaching elastic equilibrium, and (iv) detachment from the precipitate and slip to the next obstacle. From the in situ TEM results, it was confirmed that the rate limiting step of the bypass mechanism was the detachment of the dislocation from the departure side of the precipitate. In other words, the time required for dislocation climb to occur was less than the time required for dislocation bowing and detachment.

Häussler et al. also found that in a Ni-base superalloy at elevated temperatures, the rate limiting step of dislocations passing an oxide is the pinning at the interface [26]. The addition of  $Y_2Ti_2O_7$  hard and non-shearable incoherent oxide particles inhibits the motion of dislocations, though how this occurs was seen to depend on the test temperature. At low temperatures, Orowan looping mechanism dominated, while at higher temperatures, dislocation climb was prevalent. Again, dislocation climb was not found to be the rate limiting step during particle bypass. Rather, attraction between the dislocation and the particle interface was found to be the primary strengthening mechanism, imparting creep resistance to the alloy. Häussler et al. were able to directly observe this mechanism during in situ HVEM straining experiments and verify the climb and detachment mechanism at 1020 and 1165 K in Inconel MA 754 Ni superalloy. At elevated temperatures, they found strain-rate dependent dislocation behavior. At low strain-rates, it was found that detachment is the rate-limiting step and is slower than the bowing out of the dislocation. At higher strain-rates, bowing out is the slower step compared to detachment and the deformation process is smoother.

Yeh et al. found that dislocations were attracted to the precipitate interfaces in Al with Be precipitates when the samples were heated [28]. In their experiment, in situ TEM heating to 473 and 623 K was used to induce thermal stresses and drive dislocation motion. One key finding in the study was that the stress for detachment was near the Orowan stress, highlighting the attraction of the dislocations to the matrix–particle interface. The authors suggested that the interfaces relieve stress associated with the dislocation and thereby lower the energy. This is dependent on the interface characteristics, which has not been directly explored experimentally.

Dislocation–precipitate interactions in ODS intermetallics exhibit a bypass mechanism composed of dislocation climb followed by detachment, again with detachment as the rate limiting step [27]. Using in situ TEM straining experiments in HVEM at 1 MeV and a temperature of 1173 K, the deformation response of NiAl,  $Ni_3Al$ , and FeAl were investigate. Dislocations were found to split into super partial dislocations and, by measuring the distance between the leading and trailing super partial dislocations, it was seen that the distance decreased near precipitates. This suggests the interface of the precipitate is a low energy position for the dislocations and exerts an attractive force. Figure 7 is a weak-beam dark field micrograph of a super dislocation slipping through the matrix and restricted by several precipitates. Dislocation bowing between oxide particles is apparent in the micrograph, indicating that the oxides are pinning the dislocations during glide. As the dislocation interactions were observed in real time, the time-resolved position data of the lead and trailing partial dislocations could be tracked individually. These data are shown

**Fig. 7** Dissociated lattice dislocation in  $\text{Ni}_3\text{Al}$  ODS alloy propagating through a field of precipitates. The dislocation is blocked at several precipitates along its length and is bowed out between them (Image used with permission from [27])

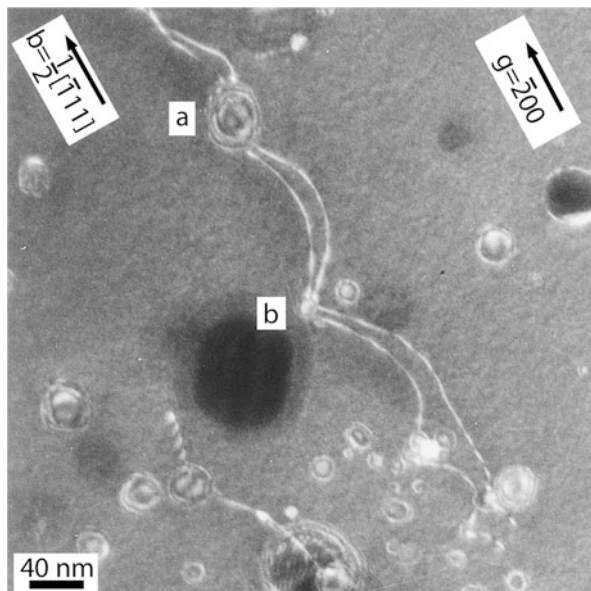
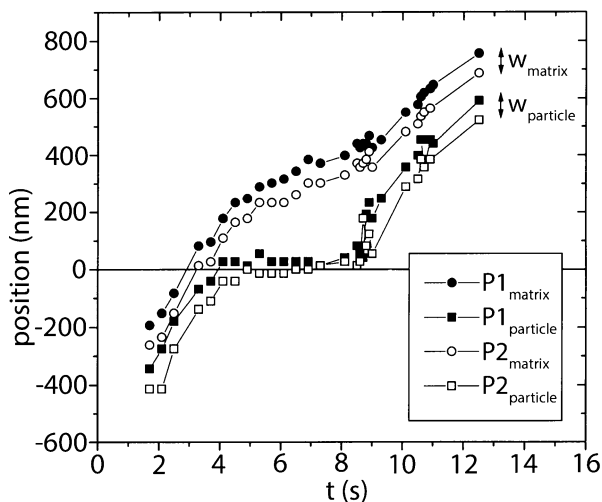


**Fig. 8** Position as a function of time for the leading and trailing partial dislocations P1 and P2, black and white shapes, respectively. Two dislocation line segments, the first is in the matrix and second in contact with the particle and labeled as such. The notable feature is between 4 and 8 s, the leading and trailing partial dislocations have a nearly constant position and have a smaller separation (Image used with permission from [27])



graphically in Fig. 8. Notably, the propagation of both the leading and trailing dislocations was inhibited by the particle, resulting in a decrease in their separation distance as they neared the particle interface.

Praud et al. investigated the active deformation mechanisms in a Fe-14Cr ODS alloy from 293 to 773 K [29]. During in situ TEM straining at 773 K, they found significant grain boundary source activity as well as grain boundary fracture. Straining at lower temperatures, 293 and 673 K, they found that the importance of



grain boundary sources was diminished. Dislocation pinning and Orowan bypass mechanisms at the oxides were prevalent.

Finely dispersed Cu precipitates in Fe, though not oxides, can be investigated using similar approaches. Nogiwa et al. investigated the impact of precipitate size on strengthening at room temperature by using heat treatments of 20 min and 10 h at 798 K of Fe with Cu additions [30]. Without the heat treatment, the precipitates were predicted to be less than 0.6 nm and with heat treatments, less than 4 nm. This was not confirmed in the experiments. They found that, when no heat treatment was used, dislocation pinning was not observed. In the heat-treated samples, dislocations were pinned at precipitates, with the pinning strength higher in the sample annealed for 10 h. However, the general strength increase due to the precipitates was consistent when measuring the bow-out of dislocations before detachment from the precipitates for each case. Comparing the direct observations of dislocation bowing, the obstacle strength parameter of the precipitates was found using [31]:

$$\Delta\sigma_c = T\Delta\tau_c = T(\mu b/L) \cos(\varphi_c/2)^{3/2} (1 - \varphi'/5\pi)$$

Where  $\Delta\sigma_c$  is the tensile stress increase,  $\Delta\tau_c$  is the hardening,  $T$  is the Taylor factor,  $\mu$  is the shear stress,  $b$  is the dislocation Burgers vector, and  $\varphi$  is the breaking angle between the dislocation and the precipitate. The obstacle strength was in good agreement with the increase in strength measured by tensile testing. Tougou et al. also used this approach to measure the obstacle strength parameter in a V-4Cr-4Ti alloy with 4 nm Ti(OCN) precipitates at room temperature [32]. Though the studies confirmed the applicability of the equation, it is limited by the necessity to conduct in situ TEM experiments for accurate dislocation bowing measurements.

### 3.3 Irradiation-Induced Defects

Irradiation of materials with energetic particles is known to result in the formation of defects, including perfect and faulted dislocation loops, stacking-fault tetrahedra, and voids. The density of these defects increases with dose, usually measured in displacements per atom (dpa), increasing the strength and decreasing the ductility of the irradiated material. Dislocation interactions with irradiation-induced defects have been found to result in strain localization into dislocation channels, or channels through the material in which the barrier to glide is lower than the surrounding matrix [33–36]. Despite the importance of these channels in modelling deformation behavior, the specific channel formation mechanisms, including channel nucleation and broadening, are not clear from post mortem characterization and remain controversial in the literature.

Dislocation channel formation has been observed in in situ TEM experiments in 304 stainless steel [37, 38] and Cu [39] irradiated with ions as well as Mo and Fe–Cr–Ni irradiated with protons [40, 41]. Suzuki et al. investigated dislocation channel formation in 99.99% pure Mo and a Fe–Cr–Ni alloy, covering both BCC and FCC, respectively [40, 42, 43]. Their studies were conducted in a HVEM to



observe thicker, non-perforated samples. In 1  $\mu\text{m}$  thick Mo specimens, dislocation channel formation corresponded to slip on a specific slip plane by dislocations clearing the irradiation defects. Though the width of the channels was observed to saturate, formation and thickening of channel walls, consisting of dislocation tangles, continued with increasing strain. It was found that the sample thickness changed the behavior such that thinner Mo samples, less than 0.5  $\mu\text{m}$ , did not form dislocation channels but instead a uniform decrease in loop number density occurred. Other studies on FCC materials, including Cu and 304 stainless steel, observe defect free channel formation at lower thicknesses [37, 39].

Studies on the FCC metals conducted after that of Suzuki et al. more closely investigated the channel formation mechanisms. Robach et al. combined in situ straining and ion irradiation of Cu in the TEM [39]. They observed that glissile dislocations present before irradiation were pinned by the irradiation defects and post-irradiation slip of those dislocations was limited. Channel formation was the result of new dislocations generated at grain boundary and crack tip sources. As the dislocations slipped and encountered the irradiation defects, bowing occurred and the breakaway stress was found to be between 15 and 175 MPa with a mode around 40 MPa. Dislocation glide was observed to eliminate the irradiation induced defects, leading to the formation of defect free, or at least partially cleared, channels. During channel formation, it was found that the passage of a single dislocation was insufficient to clear an irradiation-induced defect from the matrix. Instead, the passage of multiple defects was required. Double cross-slip of screw dislocations was observed frequently and found to widen the dislocations channels. Similar findings are available for 304 stainless steel, with the additional observation that dislocation source widening at grain boundaries was also found to contribute to channel widening [37, 38].

---

## 4 Dislocation Interactions with Isolated Obstacles

Several studies have used in situ TEM deformation experiments to investigate the interactions of dislocations with isolated defects, determining how characteristics of the defects affect the dislocation interaction mechanisms. TEM experiments have the advantage of allowing the characterization of the crystallographic details of interactions including determining the Burgers vectors of dislocations. Some applications of in situ TEM deformation techniques include dislocation interactions with irradiation produced dislocation loops, stacking fault tetrahedra, and precipitates. This section focuses on the specific interaction mechanisms with isolated defects, as opposed to the previous section which dealt with interactions with defect fields.

### 4.1 Dislocation Loops

Dislocation loops can be generated during deformation, heating, or irradiation of metals and alloys. These loops can act as obstacles to dislocation motion, traps for solute particles, and nucleation sites for additional dislocation activity.

Dislocation–loop interactions can modify the dislocation loop character, either through a change in Burgers vector or via an unfauling reaction. In an irradiated BCC Fe–Cr alloy, in situ TEM deformation experiments showed that loops with Burgers vector  $a\langle 100 \rangle$  could be transformed to loops with Burgers vector  $\frac{a}{2}\langle 111 \rangle$  by interacting with a gliding dislocation [44]. This could be achieved by the dislocation reaction  $a[100] + \frac{a}{2}[\bar{1}11] = \frac{a}{2}[111]$ . The importance of this is the  $a\langle 100 \rangle$  type loops are immobile while  $\frac{a}{2}\langle 111 \rangle$  are mobile and more energetically favorable. In a FCC Fe–Cr–Ni alloy, Suzuki demonstrated that loop unfauling can occur according to  $\frac{a}{2}[\bar{1}\bar{1}0] + \frac{a}{3}[111] \rightarrow \frac{a}{6}[\bar{1}\bar{1}2]$  [43].

Drouet et al. demonstrated the ability of glissile dislocations to interact with and incorporate vacancy loops during deformation. They observed dislocation glide during in situ TEM deformation of an ion-irradiated Zircaloy-4 sample at 773 K [45]. A dislocation with Burgers vector  $\frac{a}{3}[\bar{2}110]$  gliding on the pyramidal plane was seen to interact with a vacancy loop with the same Burgers vector (Fig. 9). This interaction was also simulated using dislocation dynamics. The lattice dislocation encountered the vacancy loop in frame (b) which was then incorporated into the dislocation in frames (c) and (d). Incorporation of the vacancy loop resulted in the formation of a helical segment on the dislocation, increasing its resistance to glide. This interaction mechanism would not be observable by post mortem analysis.

## 4.2 Stacking Fault Tetrahedra

Stacking fault tetrahedra from irradiation or quenching have also been investigated in regards to how dislocations interact with them. Several types of interactions of dislocations with stacking fault tetrahedra have been observed, including shearing and shrinking of tetrahedra and cross-slip facilitated dislocation bypass mechanisms.

Matsukawa et al. investigated dislocation interactions with stacking fault tetrahedra in Au and found that dislocations could shrink the tetrahedra [46]. In some cases, the passage of several dislocations was required to clear a stacking fault tetrahedron while in other cases it only required one dislocation. Figure 10 shows an example of dislocations cutting through and collapsing a tetrahedron. The authors suggested that shearing of the tetrahedron results in an unstable atomic configuration, collapsing the base portion of the sheared tetrahedron. The top portion of the tetrahedron and a stable Frank loop, in addition to the glissile dislocation, remained in the matrix after the interaction. The authors acknowledged the mechanism is still unclear for clearing stacking fault tetrahedra as it is known tetrahedra can be completely removed by interactions with lattice dislocations. Different mechanisms were proposed by Robach et al. that include collapsing a tetrahedron to a glissile dislocation loop as well as simple shearing of the tetrahedron [47]. Both mechanisms were based on observations from in situ straining TEM experiments but disagreed with molecular dynamics simulations of the same interaction.

At elevated temperatures, 573–773 K, dislocations have been observed to bypass stacking fault tetrahedra via cross-slip or to annihilate, or partially annihilate, the

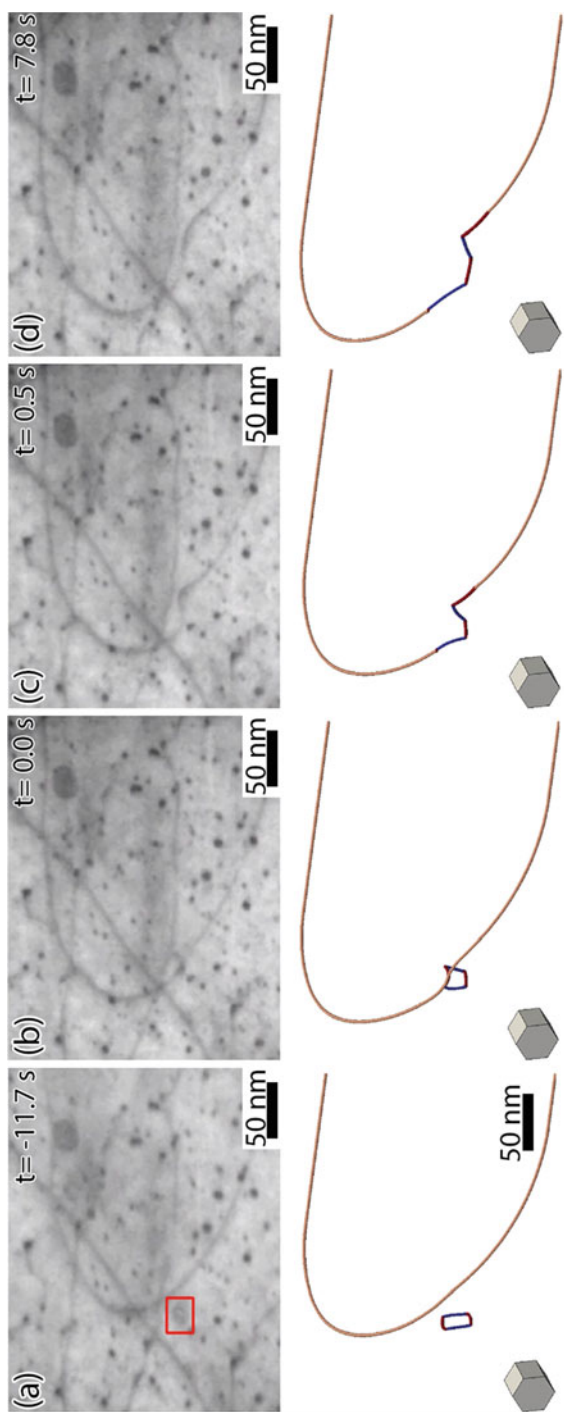


**Fig. 9** Time resolved transmission electron microscope micrographs of in situ straining experiment in Zr irradiated Zircaloy-4 in the left column. Dislocation dynamics simulation of the interaction of a dislocation with Burgers vector or  $\frac{2}{3}[2110]$  on the pyramidal plane  $(0111)$  with vacancy loop with Burgers vector of  $\frac{2}{3}[2110]$  which is in good agreement with the interaction observed in the TEM experiment (Image used with permission from [45])

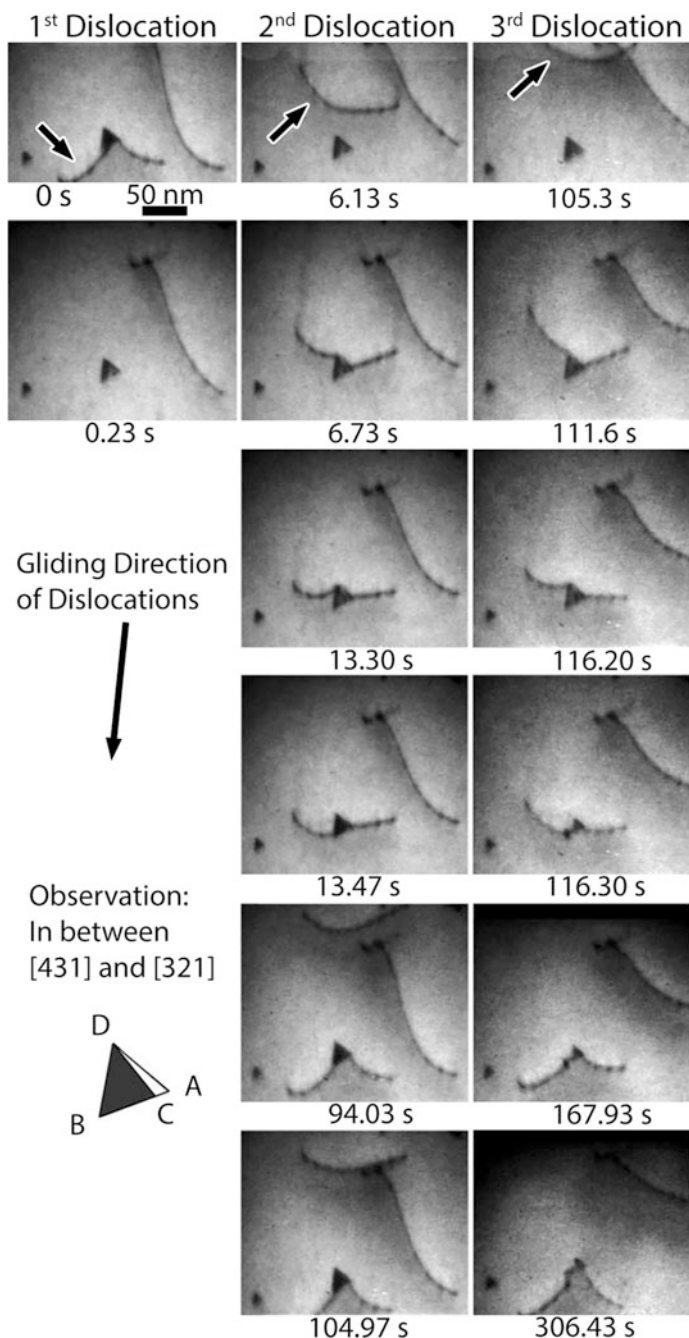


**Fig. 10** Time resolved TEM micrographs of interactions of three lattice dislocations with a stacking fault tetrahedron. The first, second and third dislocation interactions are observed in the left, middle and right columns, respectively. Collapse of the tetrahedron occurs after the third dislocation (Image used with permission from [46])

tetrahedra upon contact in Au [48]. The observed mechanism was found to depend on the location at which the dislocations intersected a tetrahedron. When encountering the stacking fault tetrahedra at one of the edges, cross-slip to avoid the obstacle occurred. Whereas encountering a tetrahedron at one of the faces resulted in partial or complete annihilation of the tetrahedron. The variety of the interactions demonstrates the complexity of lattice dislocation interactions with stacking fault tetrahedra. It also shows the need to progress the characterization of these interactions to four dimensions, where time and all three spatial dimensions are resolved.

### 4.3 Precipitates

Interactions between low angle grain boundaries, comprised of multiple dislocations, as well as individual dislocations with precipitates have been observed during in situ TEM deformation. There are several factors that impact how dislocations interact with precipitates, including size and coherency of the precipitate, environment temperature, and intersection location.

During in situ straining of an Al-4 Mg-0.3Sc alloy at 733 K, Clark et al. observed individual dislocations as well as mobile low-angle grain boundaries interacting with precipitates [49]. They found that as low-angle grain boundaries intersected large precipitates, the boundary structure was ruptured, resulting in the boundary breaking into smaller segments. Conversely, interactions with small precipitates did not alter the boundary structure. Clark et al. further studied the same alloy at 673 K and found that, when gliding dislocation arrays encountered large precipitates, the individual dislocations encountering the precipitates interacted with the precipitate–matrix interface dislocations [50]. As the dislocation array passed, dislocations remained pinned at the precipitate. This interaction is shown in the time-resolved series of electron micrographs presented in Fig. 11. Breakup of the low-angle grain boundaries was not reported. Single dislocation interactions with the large incoherent  $\text{Al}_3\text{Sc}$  precipitates at 673 K were observed to be attractive or repulsive. The difference was attributed to the relationship of the matrix and particle, including differences in: (i) lattice parameter, (ii) shear modulus, (iii) Poisson's ratio, and (iv) coefficient of thermal expansion. The location of intersection was also found to be an important factor dictating whether the interaction was repulsive or attractive.

---

## 5 Dislocation–Grain Boundary Interactions

One of the primary factors dictating the mechanical properties of a material is the distribution of grain boundaries. Grain boundaries have long been known to strengthen materials as well as to influence the corrosion resistance, fatigue damage nucleation, embrittlement, and susceptibility to irradiation damage. Much of this influence can be related to the stress state surrounding grain boundaries and how it evolves during dislocation–grain boundary interactions. Changes in matrix and boundary properties can vary the rate limiting step affecting the transfer of

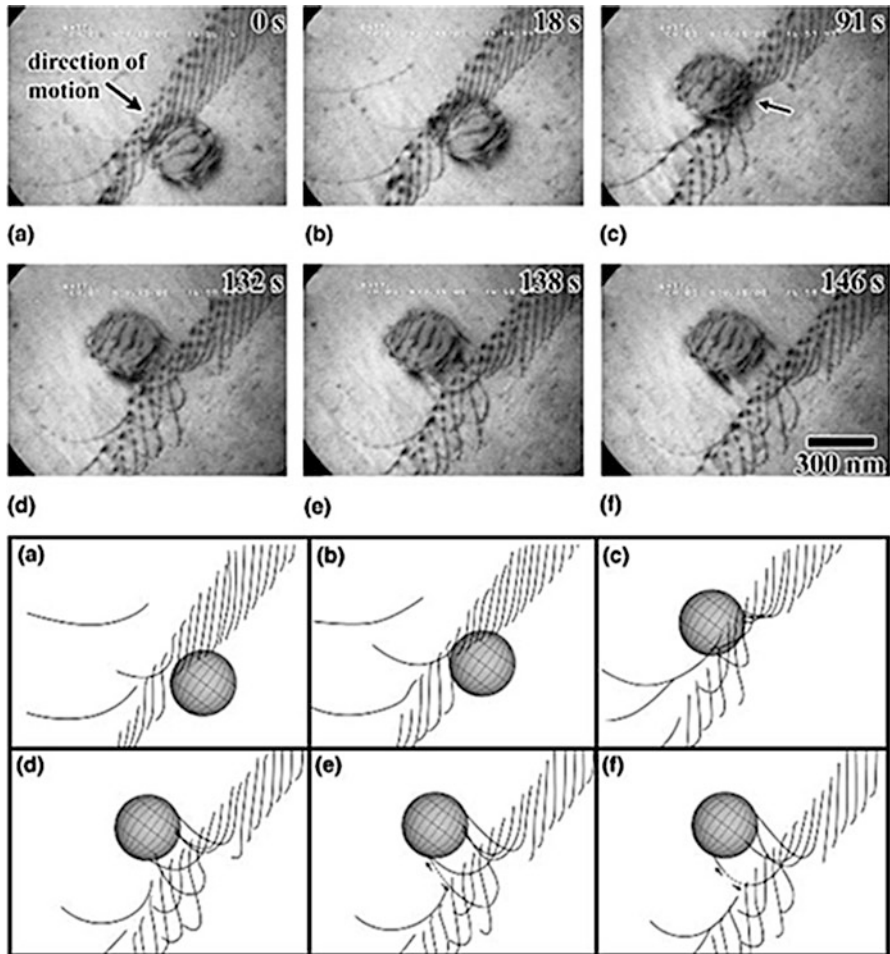


**Fig. 11** Time-resolved electron micrographs of a dislocation array interacting with an  $\text{Al}_3\text{Sc}$  precipitate at 673 K. Corresponding diagram of the interaction below the micrographs (Image used with permission from [50])

dislocations across the boundary between absorption limited, nucleation limited, or propagation limited, with each having a different influence on the stress state around the boundary. These dislocation transfer mechanisms can have profound influences on the material response to external stimuli and environments.

In situ TEM deformation remains the only experimental technique capable of resolving unit processes occurring during dislocation–grain boundary interactions and has been instrumental in identifying factors affecting each stage of the interaction, shedding light on material behavior under a variety of ambient or extreme conditions. Specifically, in situ TEM deformation seeks to identify (1) the primary factors dictating the interaction (giving access to predictive capabilities) and (2) the

rate limiting step in the interaction; see review by Kacher et al. [51] and references therein. The following sections will investigate dislocation–grain boundary interactions in different environments and microstructures and comment on the resultant variations in transfer mechanisms with an emphasis on the local stress state.

## 5.1 General Characteristics

Dislocation–grain boundary interactions can be separated into four stages of evolution: initial dislocation pileup at the boundary, absorption of the dislocation into the boundary structure, nucleation of a dislocation from the grain boundary, and propagation of the dislocation from the boundary. At every stage of the interaction, the net Burgers vector of the system must be conserved, either through the complete transfer of the dislocation across the grain boundary, incorporation of the Burgers vector into the grain boundary through the creation of an extrinsic grain boundary dislocation or its conversion to intrinsic grain boundary dislocations, back emission of a dislocation into the original grain, or, as is most common, some combination of these mechanisms. For example, depending on geometric and environmental considerations, a dislocation, once absorbed, can glide along the boundary plane, instigate the nucleation of a dislocation into the original grain (back-emission) or into the neighboring grain (forward emission), or retain its character and transfer into the neighboring grain via a cross-slip interaction (direct transfer) [51–53]. Examples of these interactions are shown in the electron micrographs presented in Fig. 12. Grain boundary characteristics, geometric factors, defect state of the matrix, test temperature, and test environment can all influence the relative importance of each stage of the interaction.

In situ TEM deformation experiments have been instrumental in establishing broad predictive criteria for understanding dislocation–grain boundary interactions. By fully characterizing the incoming and outgoing dislocation systems involved in an interaction as well as the crystallographic relationship between the two grains, it has been shown that dislocation–grain boundary interactions satisfy the following three criteria [53]:

1. The angle between the traces of the incoming and outgoing slip systems in the grain boundary should be minimized;
2. The magnitude of the Burgers vector of the residual grain boundary dislocation ( $|\mathbf{b}_{res}|$ ) should be minimized;
3. The resolved shear stress acting on the outgoing slip system should be maximized.

Of the three, the magnitude of the Burgers vector of the residual grain boundary dislocation has been found to have the largest influence. Criterion 1 has been found to only be important in limited cases where the slip planes of the incoming and outgoing dislocation systems aligned exactly in the boundary, as may be encountered in the transfer of screw dislocations across twin boundaries. The magnitude of



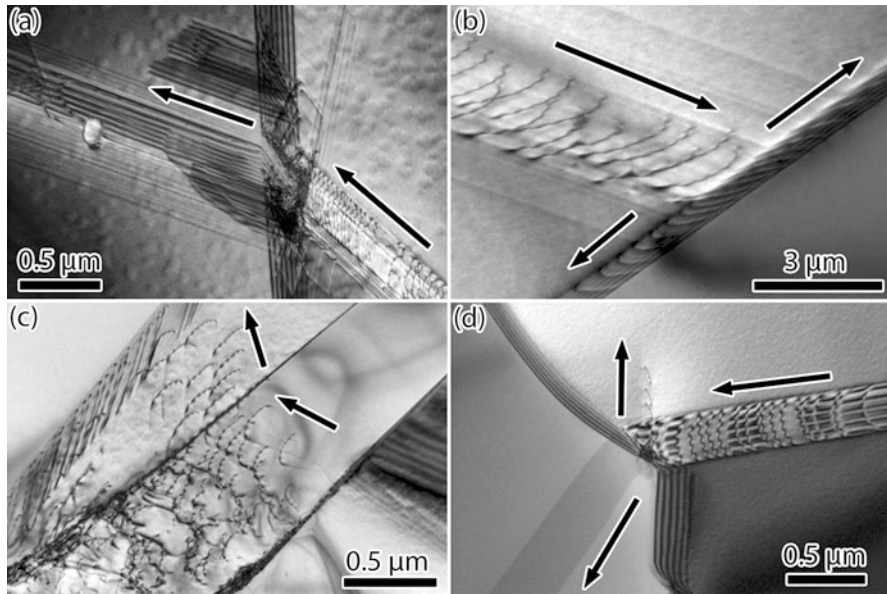


**Fig. 12** Possible dislocation–grain boundary interactions. (a) Dislocation absorption into and nucleation from a random high angle grain boundary in 304 stainless steel. (b) Dislocation absorption into a coherent twin boundary in 304 stainless steel. (c) Direct transfer of dislocations across a coherent twin boundary in commercially pure  $\alpha$ -Ti. (d) Dislocations interacting with a random high angle grain boundary in 304 stainless steel showing absorption and both forward and back emission. Arrows indicate direction of dislocation propagation

the resolved shear stress acting on the emitted dislocation system was found to be important only in that it must be of sufficient magnitude to propagate the dislocations away from the boundary. In coarse-grained systems with little prior damage, the stress needed is relatively low, diminishing the importance of Criterion 3. These criteria were originally established in coarse-grained, FCC materials under quasi-static loading conditions, though experiments have confirmed their validity in additional crystal systems [53, 54].

## 5.2 Temperature Effects

Increasing the environment temperature during material testing increases the likelihood of thermally activated events such as dislocation cross-slip and climb occurring and increases the rate of kinetic processes. Similarly, elevated temperatures can provide energy to overcome barriers to dislocation events associated with grain boundary interactions, such as absorption and nucleation. Kacher et al. directly compared the interaction of dislocations with a coherent twin boundary in austenitic stainless steel during in situ TEM deformation by first, observing the interaction under ambient conditions, relieving the applied stress, increasing the temperature to 673 K,

and reapplying the stress to reinitiate the interaction [55]. They found that, at elevated temperatures, the barrier to dislocation transfer across the boundary decreased and additional dislocation systems were activated, increasing the complexity of the interaction. The interaction followed the same criteria outlined in the previous section at both ambient and elevated temperatures, suggesting that the temperature primarily influenced the rate of the interaction but not the governing mechanisms.

In investigating dislocation–grain boundary interaction with random high-angle grain boundaries at elevated temperatures, Kacher et al. found that the barrier to absorption of high angle grain boundaries to impinging dislocations was significantly reduced [55]. The dislocation nucleation process at the boundary was also somewhat altered in relationship to ambient-temperature interactions, with a significant increase in partial dislocation activity observed. Figure 13a, b shows an example of dislocations interacting with a random high-angle grain boundary during deformation at 673 K. Figure 13a shows that a large number of dislocations have piled up at the grain boundary. This initial pileup occurred prior to the temperature increase; the initial stages were not captured. Diffraction contrast imaging suggests that the dislocation pileup led to a large concentration of elastic strain at the interaction point. To avoid the concentrated elastic strain and the associated stress fields, a few of the dislocations were seen to cross-slip from the dominant slip system and, after propagating a few hundred nanometers, cross-slipped back onto a parallel slip plane. The interaction of cross-slipped dislocations with the grain boundary occurred without the stress field associated with dislocation pileups. That is, the external load was the primary driver for the interaction. The absorption process into the boundary plane occurred quickly with no dislocation pileup needed to initiate the absorption process. Figure 13b shows that each absorbed dislocation resulted in the emission of a lead partial dislocation into the neighboring grain. The emitted partial dislocations did not propagate far from the boundary plane but instead were anchored by the trailing partial dislocation, resulting in an elongated faulted region extending from the boundary to the lead partial dislocation.

A second high-temperature interaction, shown in Fig. 13c, d, similarly demonstrated the low-barrier of dislocation absorption into the boundary plane. The progress of a single dislocation was tracked as it approached the grain boundary (Fig. 13c). Upon reaching the grain boundary, the dislocation was absorbed and immediately after, to within the 0.1 s, a lead partial dislocation was emitted into the neighboring grain. Similar to the previous interaction, the trailing partial dislocation remained in the boundary and a faulted region extended to the lead partial dislocation.

In both interactions shown in Fig. 13, the dislocation system activated at the boundary minimized  $|\mathbf{b}_{res}|$ . However, this minimization occurred differently at different stages of the interaction due to the elevated activity of partial dislocations. In the initial stages of the interaction, dislocation emission from the boundary was dominated by lead partial dislocations, with the trailing partial remaining in the boundary. Characterization of the Burgers vectors of the incoming and outgoing dislocations showed that, in both interactions, emission of the trailing partial dislocation significantly increased the value of  $|\mathbf{b}_{res}|$ . The associated large energy barrier was hypothesized to account for the elongated faulted regions extending from the boundary.

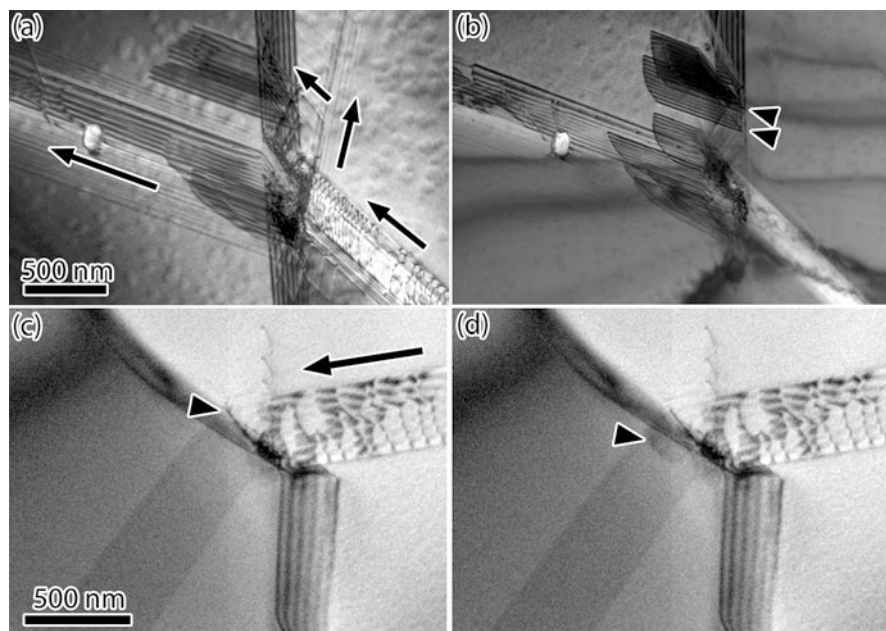


**Fig. 13** Dislocations interacting with random, high-angle grain boundaries at 400 °C during in situ TEM deformation. (a, b) Images of the same interaction taken using two different diffraction conditions. Arrows indicate direction of dislocation propagation. Arrowheads in (b) indicate where lead partial dislocations have nucleated at and propagated from the grain boundary. (c, d) Two frames of a video taken 0.1 s apart. Arrow indicates direction of dislocation propagation. The arrowheads track a single interaction as a perfect dislocation is absorbed into the boundary and a lead partial dislocation nucleates at the boundary immediately after

### 5.3 Coherent Twin Boundaries

Coherent twin boundaries present a special case of dislocation–grain boundary interactions for a number of reasons: (1) in FCC materials, the twin plane is also a dislocation glide plane, (2) the crystal symmetry across the twin boundary can allow perfect transfer of the Burgers vector, (3) in cases when the crystal geometry does not allow perfect transfer of the Burgers vector, the residual grain boundary dislocation often takes the form of a partial dislocation glissile on the twin boundary plane, and (4) coherent twin boundaries are exceptionally low-energy, potentially increasing the barrier to dislocation transmission (as shown computationally in ([56])). As a result, geometric factors, specifically the relationship between the dislocation Burgers vector, line direction, and boundary plane, have a much larger influence in how the interaction progresses than in more general dislocation interactions with high angle grain boundaries.

Figure 14 illustrates the effect that the relationship between the twin plane and the incoming dislocation character can have on dislocation–twin boundary interactions in FCC materials [55]. In this case, two different systems of perfect dislocations in an austenitic stainless steel sample impinging on a coherent twin boundary during in situ

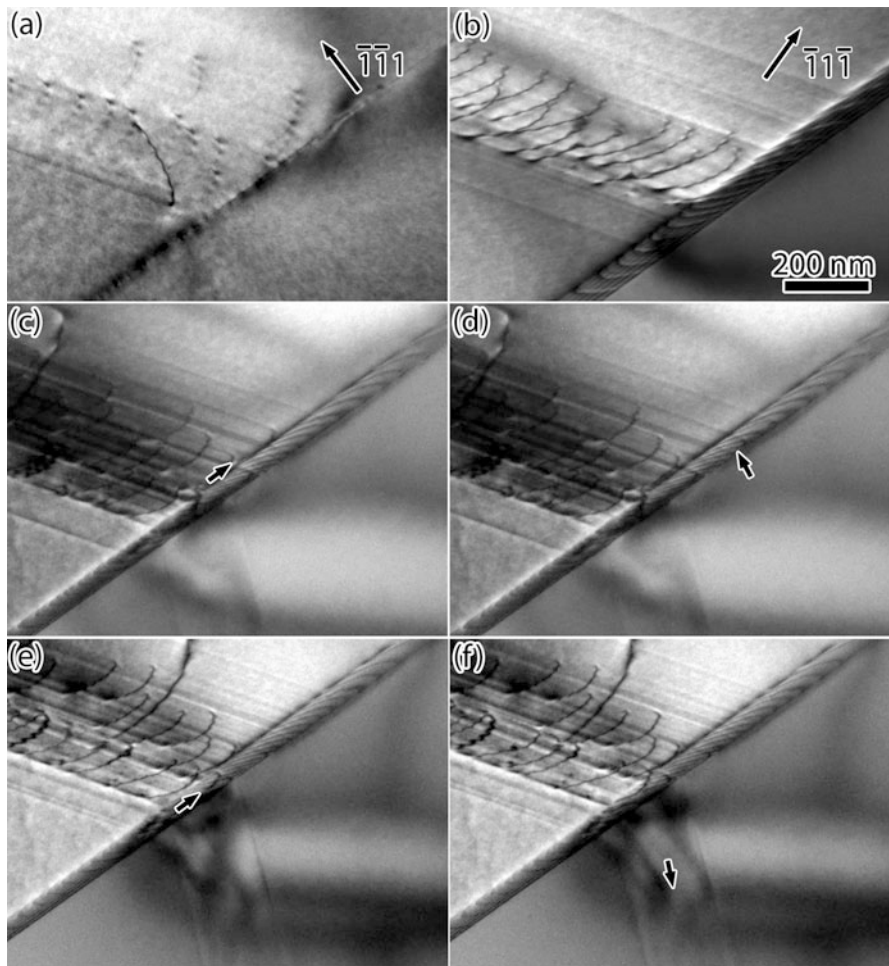


**Fig. 14** Dislocations interacting with a coherent twin boundary during in situ TEM deformation of 304 stainless steel at 673 K. (a, b) Image of interaction site under two different diffraction conditions showing presence of distinct slip systems. (c, d) Interaction of a dislocation from system (b) showing impingement on and incorporation into the boundary. Arrows track an individual dislocation immediately before (c) and after (d) absorption into the boundary plane. (e, f) Interaction of a dislocation from system (a) showing impingement on, nucleation, and propagation from the boundary. Arrows indicate a dislocation immediately prior to being absorbed into the boundary (e) and its direction of motion after emission from the boundary (f) (Image sequences are separated by 0.1 s)

TEM deformation at 673 K. The Burgers vector of the first system dislocations, visible in Fig. 14a, allows them to either glide in the twin boundary plane or completely transfer across the boundary plane without leaving a residual twin boundary dislocation. Figure 14c, d shows that, upon impinging on the boundary plane, they were absorbed quickly and glided along the twin plane as perfect dislocations; an arrow

tracks a single dislocation immediately before (Fig. 14c) and after (Fig. 14d) it is absorbed into the boundary plane. The Burgers vector of the second system, visible in Fig. 14b, does not allow glide in the twin plane. In Fig. 14e, f, a dislocation from the second system is seen impinging on the twin plane. The dislocation was absorbed quickly into the twin plane and immediately, to within 0.1 s, a dislocation was emitted into the neighboring grain; the arrow in Fig. 14e indicates the location of the dislocation immediately prior to being absorbed and the arrow in 14f indicates the direction of dislocation motion after emission from the boundary.

As the interaction progressed, the density of extrinsic dislocations in the twin boundary continued to increase, raising the stress levels in the boundary. The effect of this buildup of dislocations is apparent when the associated stress reaches a critical level, shown in Fig. 15. Initially, the extrinsic grain boundary dislocations continued to glide away from the interaction point; this is apparent from the curvature of the individual dislocations (Fig. 15a). However, an uncharacterized structural transition took place at the interaction point that released the dislocations from the boundary plane, relieving the stress acting on the dislocations. As a result, the dislocations reverse course and rapidly exit the boundary at the interaction point; this course reversal is apparent from the reversed curvature of the individual dislocations seen in Fig. 15b. This behavior could have important implications in failure mechanisms at twin boundaries.

Figure 16a demonstrates the ability of dislocations in certain systems to transfer across a twin boundary via simple cross-slip [54]. This image shows a-type screw dislocations in  $\alpha$ -Ti gliding on a prismatic plane interacting with a  $\{1\bar{1}02\}$ -type twin boundary. The prismatic planes aligned on either side of the boundary and the crystallographic relation across the boundary allowed perfect transfer of the Burgers vector of the dislocations; this is evident from a three-dimensional dislocation model constructed from an electron tomogram of the interaction. In situ observations of the dislocation glide showed that the twin boundary posed a very low barrier to slip transmission. Some dislocation trapping in the boundary plane is evident from the model. This is most likely due dislocation constriction prior to cross-slip.

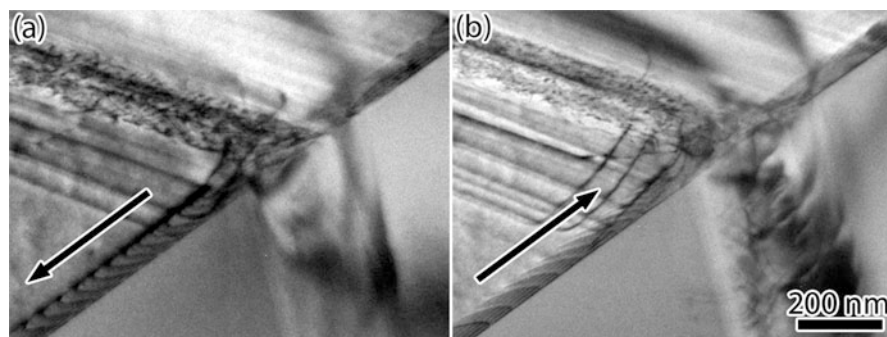
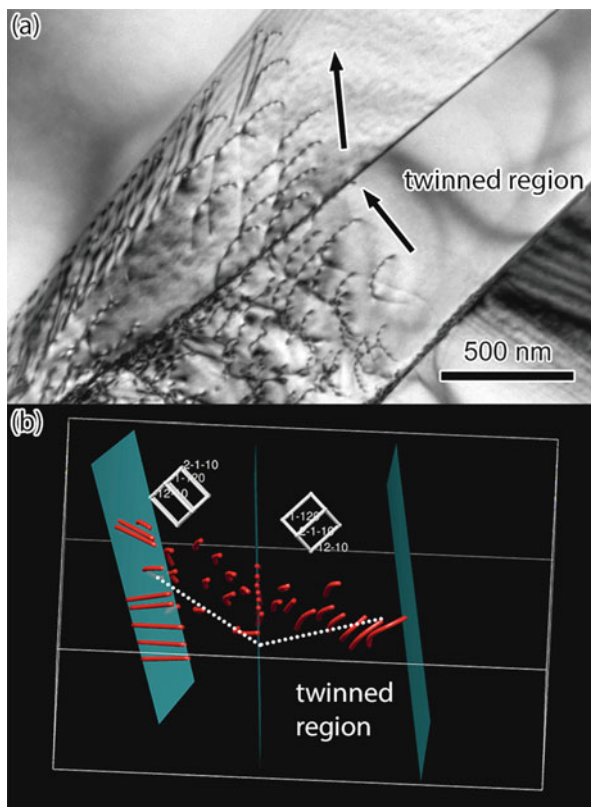


**Fig. 15** Dislocation glide in the plane of a coherent twin boundary during in situ TEM deformation at 673 K. Dislocation glide reversed at a critical point between (a) and (b). 2.6 s elapsed between frames.



**Fig. 16** (a) TEM micrograph of dislocations interacting with a twin boundary in  $\alpha$ -Ti. Arrows indicate direction of dislocation propagation. (b) Dislocation model of the interaction constructed from an electron tomogram. Coordinate systems aligned with the crystallographic crystal axes are included in each crystal region. Dotted lines indicate the slip plane trace, showing alignment at the twin boundary plane



#### 5.4 Propagation Limited Systems: Irradiated Materials

Bombardment of metallic alloys by energetic particles is known to cause microstructural changes, including the formation of nanoscale dislocation loops distributed throughout the matrix. The interaction of dislocations with these defects are discussed in depth in an earlier section, though it is appropriate here to note that these nanoscale defects act as barriers to dislocation propagation, effectively hardening the matrix and subsequently having a significant effect on dislocation–grain boundary interactions.

Figure 17 shows three separate examples of dislocation systems interacting with grain boundaries in austenitic stainless steels during in situ TEM deformation at 673 K [37, 38, 41, 57]. In Fig. 17a, a dislocation system is seen interacting with a low-angle grain boundary [37]. The intersection of the dislocation system resulted in a large strain concentration at the boundary and the emission of dislocations into the neighboring grain. Initially, perfect dislocations were emitted in two different slip systems, with one of the systems being significantly more active than the other. After the emission of  $\sim 20$  dislocations, the more active system transitioned from the emission of perfect dislocations to partial dislocations. Due to the barrier presented

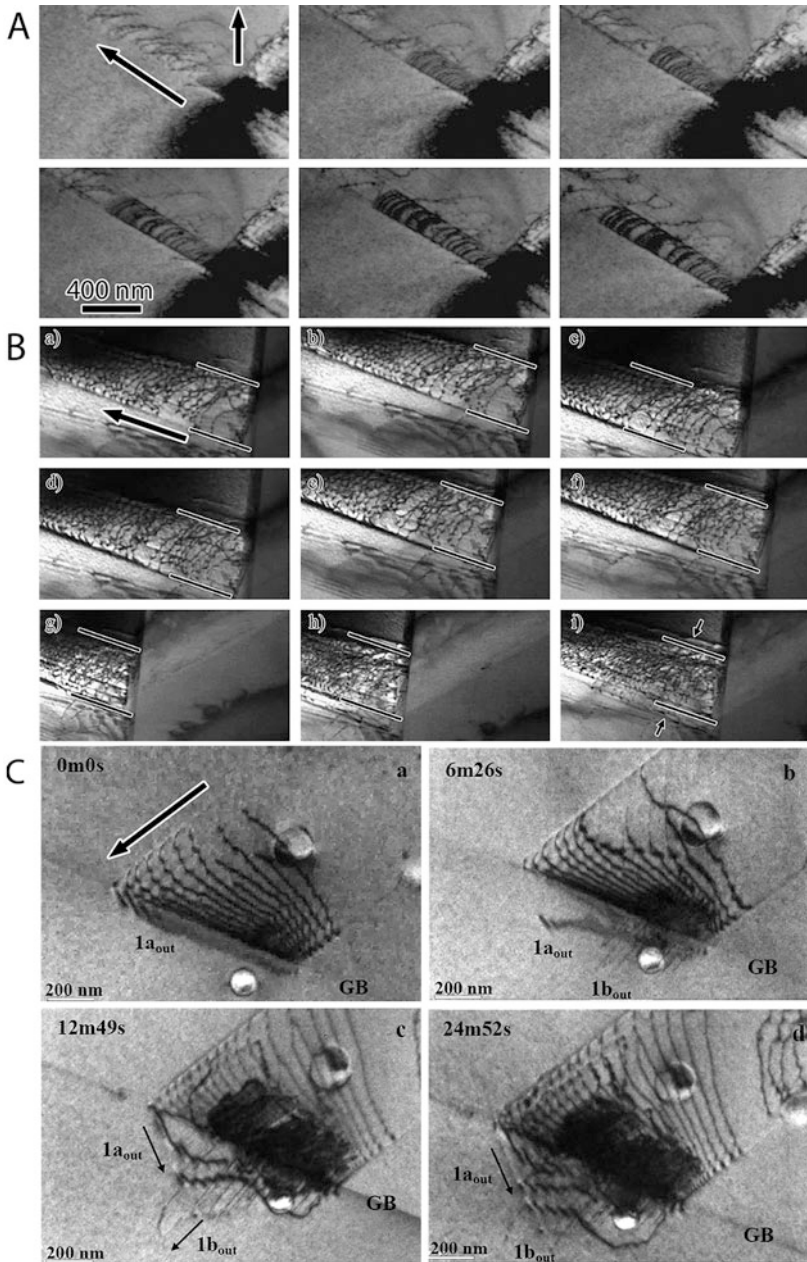


**Fig. 17** Dislocation–grain boundary interaction during in situ TEM deformation of ion-irradiated stainless steel samples. (a) Dislocation interactions with a low-angle grain boundaries. (b) Dislocation source widening during dislocation emission from a grain boundary (used with permission from [38]). (c) Dislocations interacting with a  $\Sigma 9$  grain boundary. Arrows indicate direction of dislocation motion (used with permission from [57])



by the dispersed irradiation-induced defects, the dislocations did not propagate easily from the boundary and formed a high density near the boundary source.

Figure 17b shows the emission of perfect dislocations from an uncharacterized grain boundary [38]. The dislocation emission resulted from the impingement of a single dislocation system. As the dislocations nucleated from the boundary, they remained tightly packed, resulting in large, internal pileups. Black lines mark the slip traces of the dislocations originally emitted from the boundary source. Over time, this source volume increased. This can be seen from the increased distance between slip traces at the boundary, indicated by arrowheads in Figure 17bi.

In the third example, shown in Fig. 17c, dislocations impinged on a  $\Sigma 9$  boundary [57]. Originally, a few partial dislocations emitted from the boundary, well aligned with the incoming dislocation system. These were soon followed by the emission of multiple perfect dislocations belonging to a different slip system. Each of these perfect dislocations originated from a different location on the boundary plane and was not able to propagate far from the boundary. Two additional dislocation systems, not visible in the video frames, also activated at the interaction site, with one system propagating through the boundary plane and the other emitted back into the original grain. The activity of these additional systems was limited in comparison to the two systems visible in Fig. 17c. To explore the micromechanics occurring during dislocation–grain boundary interactions in irradiated systems, Cui et al. characterized multiple interactions in terms of grain boundary character and dislocation slip systems. Using this information, they calculated the local stress state at the boundary using a “super dislocation” model where the incoming dislocation pileup was represented as a single dislocation at the boundary. The emitted dislocation systems were analyzed in terms of  $|\mathbf{b}_{res}|$  and the resolved shear stress, similar to the criteria proposed by Lee et al. [53]. Cui et al. found that, while  $|\mathbf{b}_{res}|$  was still the most important factor, the relative importance of the resolved shear stress condition increased. Instead of easy propagation from the boundary, the dislocations required sufficient stress to overcome the barrier posed by the defect field. They confirmed this by observing that in some cases additional dislocations had to be added to the dislocation pileup, that is, the local stress increased, before dislocations were emitted from and propagated away from the grain boundary.

Despite the differences seen in the grain boundary character, dislocation type, and loading conditions of the interactions shown in Fig. 17, the three interactions share commonalities general to dislocation–grain boundary interactions in irradiated systems. In each interaction, the irradiation damage was not seen to limit dislocation nucleation from the boundary. Propagation from the boundary, however, was restricted by the dispersed defect field. This barrier to propagation resulted in the formation of “reverse” pileups at the grain boundary. That is, a high concentration of dislocations develops at the emission side of the boundary in contrast to the rapid propagation from the grain boundary source commonly seen in unirradiated, coarse-grained materials. This effect has important implications in the local strain concentrations developing at boundaries and has been linked to irradiation assisted stress corrosion cracking [58].

In addition to the development of reverse dislocation pileups, each interaction shows significant source broadening at the grain boundary. In the interactions shown

in the series of images presented in Fig. 17a and c, this broadening occurs through the emission of multiple dislocation systems from different locations on the boundary plane. In the interaction shown in Fig. 17b, tracing of the slip traces on the foil surface shows that multiple parallel slip systems were emitted from nearby locations in the boundary. This occurs despite only a single dislocation system impinging on the grain boundary. This source broadening has important implications in understanding confined plasticity and the development of dislocation channels, key aspects of irradiation induced embrittlement, and is thought to be related to the stress concentrations associated with reverse dislocation pileups.

## 5.5 Confined Microstructure: Ultrafine Grained and Nanotwinned Materials

Efforts to fully exploit the Hall–Petch effect have led to the development of increasingly fine-grained systems. Although the dislocation transfer mechanisms across a grain boundary in ultrafine-grained materials are not expected to differ significantly from their coarse-grained counterparts, the limited volume for the development of dislocation pileups and the attendant long-range stress fields can alter the local stress state. As the deformation of nanograined materials is largely dominated by grain boundary deformation mechanisms, the discussion here is limited to nanotwinned and ultrafine-grained systems.

Under monotonic loading in an ultrafine-grained sputter-deposited Al film, Momprou et al. characterized the stresses associated with dislocation nucleation from a grain boundary and compared them with the stress needed to propagate a dislocation through the boundary plane [59]. Using dislocation curvature, they found that dislocation nucleation from a triple junction required a resolved shear stress level of 500 MPa. In comparison, the stress needed to propagate the dislocation through the boundary plane was only 157 MPa, suggesting that nucleation, rather than propagation, was the rate limiting step in the deformation process.

Momprou et al. also investigated the dislocation evolution in ultrafine-grained Al (avg. grain size was ~500 nm) produced using equal-channel angular pressing (ECAP) under multiple loading-unloading cycles [60]. They observed that for both predominately edge and screw dislocations, the initial impingement of a dislocation at a grain boundary resulted in the absorption of the dislocation at the boundary. That is, for an undamaged grain boundary, the barrier to dislocation absorption was low. Dislocation contrast in the boundary plane post-absorption was visible for tens of seconds to minutes, after which dislocation dissolution took place. During this period, the subsequent interactions of dislocations with the grain boundary were significantly influenced by the nature of the dislocation. Predominately screw-type dislocations underwent significant cross-slip due to the repulsive stress fields surrounding the absorbed dislocations. Similar to the initially absorbed dislocation, these cross-slipped dislocations were also able to incorporate into the boundary plane. Upon unloading, the dislocations remained firmly entrenched in the grain boundaries. In contrast, predominately edge-type dislocations, which are unable to

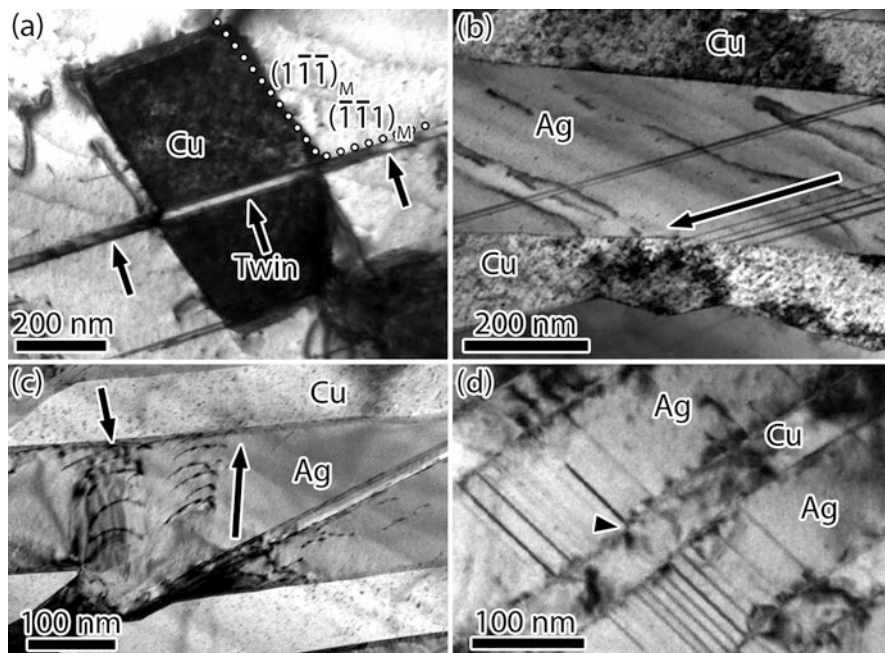


**Fig. 18** Dislocation–phase boundary interactions in a multilayer AgCu system. (a) Twin crossing cube-on-cube boundaries. Arrows indicated twin location. Twin marked by arrows. (b) Twin or stacking fault impinging on an incoherent twin interface with shared planes resulting in the emission of perfect dislocations from the interface after clearing the planar defect. Arrow indicates dislocation propagation direction. (c) Dislocation impingement on and back emission from an incoherent twin interface. (d) Twins in Ag impinging on coherent twin interface, resulting in increased elastic strain in the Cu lamella. Twin nucleation location indicated by an arrowhead [63]

cross-slip, all reached the grain boundary at the same location, resulting in the buildup of increasingly large stress concentrations. Upon unloading, these dislocations were reemitted into the original grain from the grain boundary. This behavior continued for multiple cycles, even with continued dislocation generation.

Various groups have studied the deformation of nanostructured multilayered and nanotwinned systems [61, 62]. Eftink et al. used in situ TEM deformation to investigate the interactions of dislocations with interphase boundaries in a Ag–Cu eutectic system [63]. They detailed the dislocation response at the interfaces for three different types of boundaries: cube-on-cube, incoherent twin, and coherent twin. At cube-on-cube interfaces, they found that perfect dislocations piled up at the boundary, but only limited transmission occurred. Twins and twinning dislocations, however, were seen to easily propagate across the interface, leading to twin formation in the Cu layers as well as the Ag layers (Fig. 18a). Incoherent twin interfaces posed a weak barrier to perfect dislocation propagation on the twin plane, which was continuous across the interface, resulting in some dislocation pileup formation at the interface. Twins originating from

the Ag layers and impinging on the Cu–Ag interfaces, however, did not directly transmit as transmission into the Cu layers required the leading and trailing partial dislocations to first recombine (Fig. 18b). In contrast, incoherent twin interfaces imposed strong barriers to slip transmission for dislocations on planes other than the twin plane. The activity of perfect dislocations leading to pileups at the boundaries was observed in the Ag layers, leading to absorption into the boundary, cross-slip from the pileup at the boundary intersection, and back emission from the boundary into the Ag layer, but no transmission (Fig. 18c). Interestingly, coherent twin interfaces appeared to transmit plasticity via twinning in the Ag layers and elastic strain in the Cu layers, suggesting that the layer thickness facilitated communication between the Ag layers without plastic deformation of the Cu (Fig. 18d).

Eftink et al. recently combined in situ deformation experiments with molecular dynamic computer simulations of dislocation interactions with incoherent twin interfaces in a 500 nm thick Ag–Cu layered system to explain the plastic strain recovery observed experimentally in this system [64]. They demonstrated that the plastic recovery was driven primarily by the accommodation of dislocations in the Ag and Cu layers into the interfaces. The dependence of the magnitude of the plastic recovery on the total strain was shown to be due to the formation of dislocation tangles at the higher strain as these locked the dislocations in place and prevented them from returning to and being accommodated in the interfaces. This example demonstrated the use of computer simulations to shed additional insight into dislocation interactions with interfaces.

---

## 6 Conclusion

TEM is uniquely able to image and characterize dislocation interactions in real time and at the necessary resolution to observe unit processes. In situ experiments, including deformation, irradiation, and heating, have been instrumental in elucidating complex dislocation interactions, contributing to our fundamental understanding of these interactions as well as aiding in material design and deployment. Advances in sample preparation techniques, TEM testing holders, and characterization capabilities promise further to maintain in situ TEM testing as a premier method for understanding dislocation interactions.

**Acknowledgments** For the preparation of this manuscript, the authors acknowledge financial support from Georgia Tech. (JK), Los Alamos National Security, LLC, operator of the Los Alamos National Laboratory under Contract No. DE-AC52-06NA25396 with the US Department of Energy (BPE), and US Department of Energy under award No. DE-FG02–08 ER46525 (IMR). Experimental work from the Robertson group was supported by US Department of Energy, Office of Basic Energy Sciences, Division of Materials Science, under award No. DE-FG02–08 ER46525 (radiation damage work by Cui) and US Department of Energy Office of Basic Energy Sciences, Division of Materials Science, under award No. DEFG-02-07ER46443 (slip transfer studies by Kacher and, partially, the study by Eftink on deformation across interfaces).

## References

1. Hirsch PB, Horne RW, Whelan MJ. Direct observations of the arrangement and motion of dislocations in aluminium. *Philos Mag.* 1956;86(29):4553–72.
2. Herring C, Galt JK. Elastic and plastic properties of very small metal samples. *Phys Rev.* 1952;85:1060–2.
3. Chen LY, He M-r, Shin J, Richter G, Gianola DS. Measuring surface dislocation nucleation in defect-scarce nanostructures. *Nat Mater.* 2015;14(7):707–13.
4. Lu Y, Song J, Huang JY, Lou J. Surface dislocation nucleation mediated deformation and ultrahigh strength in sub-10-nm gold nanowires. *Nano Res.* 2011;4(12):1261–7.
5. Oh SH, Legros M, Kiener D, Dehm G. In situ observation of dislocation nucleation and escape in a submicrometre aluminium single crystal. *Nat Mater.* 2009;8(2):95–100.
6. Li N, Yadav SK, Liu XY, Wang J, Hoagland RG, Mara N, Misra A. Quantification of dislocation nucleation stress in TiN through high-resolution in situ indentation experiments and first principles calculations. *Sci Rep.* 2015;5:15813.
7. Minor AM, Lilleodden ET, Stach EA, Morris JW. Direct observations of incipient plasticity during nanoindentation of Al. *J Mater Res.* 2004;19:176–82.
8. Caillard D, Martin JL. Some aspects of cross-slip mechanisms in metals and alloys. *J Phys.* 1989;50(18):2455–73.
9. Caillard D, Rautenberg M, Feugas X. Dislocation mechanisms in a zirconium alloy in the high-temperature regime: an in situ TEM investigation. *Acta Mater.* 2015;87:283–92.
10. Clouet E, Caillard D, Chaari N, Onimus F, Rodney D. Dislocation locking versus easy glide in titanium and zirconium. *Nat Mater.* 2015;14:931–7.
11. Couret A, Caillard D. An in situ study of prismatic glide in magnesium. I. The rate controlling mechanism. *Acta Metall.* 1985;33(8):1447–54.
12. Couret A, Caillard D. An in situ study of prismatic glide in magnesium. II. Microscopic activation parameters. *Acta Metall.* 1985;33(8):1455–62.
13. Farenc S, Caillard D, Couret A. An in situ study of prismatic glide in  $\alpha$  titanium at low temperatures. *Acta Metall Mater.* 1993;41(9):2701–9.
14. Naka S, Lasalmonie A, Costa P, Kubin LP. The low-temperature plastic deformation of  $\alpha$ -titanium and the core structure of a-type screw dislocations. *Philos Mag A.* 1988;57(5):717–40.
15. Kacher J, Robertson IM. In situ TEM characterization of dislocation interactions in  $\alpha$ -titanium. *Philos Mag.* 2016;96(14):1437–47.
16. Appel F, Bethge H, Messerschmidt U. Dislocation motion and multiplication at the deformation of MgO single crystals in high voltage electron microscope. *Phys Status Solidi.* 1977;42:61–71.
17. Werner M, Bartsch M, Messerschmidt U, Baither D. TEM observations of dislocation motion in polycrystalline silicon during in situ straining in the high voltage electron microscope. *Phys Status Solidi A.* 1994;146(1):133–43.
18. Baither D, Baufeld B, Messerschmidt U, Bartsch M. HVEM high-temperature in situ straining experiments on cubic zirconia single crystals. *Mater Sci Eng A.* 1997;233:75–87.
19. Messerschmidt U, Bartsch M. Generation of dislocations during plastic deformation. *Mater Chem Phys.* 2003;81(2–3):518–23.
20. Caillard D. Dynamic strain ageing in iron alloys: the shielding effect of carbon. *Acta Mater.* 2016;112:273–84.
21. Robertson IM. The effect of hydrogen on dislocation dynamics. *Eng Fract Mech.* 2001;68(6):671–92.
22. Shih DS, Robertson IM, Birnbaum HK. Hydrogen embrittlement of alpha-titanium – in situ TEM studies. *Acta Metall.* 1988;36(1):111–24.
23. Birnbaum HK, Sofronis P. Hydrogen-enhanced localized plasticity—a mechanism for hydrogen-related fracture. *Mater Sci Eng A Struct Mater Prop Microstruct Process.* 1994;A176(1–2):191–202.
24. Kacher J, Mishra RK, Minor AM. Multiscale characterization of dislocation processes in Al 5754. *Philos Mag.* 2015;95(20):2198–209.

25. Bartsch M, Wasilkowska A, Czyska-Filemonowicz A, Messerschmidt U. Dislocation dynamics in the oxide dispersion strengthened alloy INCOLOY MA956. *Mater Sci Eng A Struct Mater Prop Microstruct Process.* 1999;272(1):152–62.
26. Haussler D, Bartsch M, Messerschmidt U, Reppich B. HVTEM in situ observations of dislocation motion in the oxide dispersion strengthened superalloy MA 754. *Acta Mater.* 2001;49:3647–57.
27. Behr R, Mayer J, Arzt E. TEM investigations of the superdislocations and their interaction with particles in dispersion strengthened intermetallics. *Intermetallics.* 1999;7(3–4):423–36.
28. Yeh YH, Nakashima H, Kurishita H, Goto S, Yoshinaga H. Threshold stress for high-temperature creep in particle strengthened Al-1.5 vol-percent-Be alloys. *Mater Trans Jim.* 1990;31(4):284–92.
29. Praud M, Momprou F, Malaplate J, Caillard D, Garnier J, Steckmeyer A, Fournier B. Study of the deformation mechanisms in a Fe-14% Cr ODS alloy. *J Nucl Mater.* 2012;428(1–3):90–7.
30. Nogiwa K, Yamamoto T, Fukumoto K, Matsui H, Nagai Y, Yubuta K, Hasegawa M. In situ TEM observation of dislocation movement through the ultrafine obstacles in an Fe alloy. *J Nucl Mater.* 2002;307:946–50.
31. Foreman AJE, Makin MJ. Dislocation movement through random arrays of obstacles. *Philos Mag.* 1966;14(131):911–24.
32. Tougou K, Nogiwa K, Tachikawa K, Fukumoto K. Tensile testing study of dynamic interactions between dislocations and precipitate in vanadium alloys. *J Nucl Mater.* 2013;442(1–3):S350–3.
33. Cole JJ, Bruemmer SM. Post-irradiation deformation characteristics of heavy-ion irradiated 304L SS. *J Nucl Mater.* 1995;225:53–8.
34. Sharp JV. Correlation between cleared channels and surface slip steps in neutron irradiated copper crystals. *Radiat Eff.* 1972;14(1–2):71–5.
35. Tucker RP, Wechsler MS, Ohr SM. Dislocation channeling in neutron-irradiated niobium. *J Appl Phys.* 1969;40(1):400–8.
36. Foreman AJE, Sharp JV. A mechanism for the sweeping-up of loops by glide dislocations during deformation. *Philos Mag.* 1969;19:931–7.
37. Kacher J, Liu GS, Robertson IM. In situ and tomographic observations of defect free channel formation in ion irradiated stainless steels. *Micron.* 2012;43(11):1099–107.
38. Briceno M, Fenske J, Dadfarnia M, Sofronis P, Robertson IM. Effect of ion irradiation-produced defects on the mobility of dislocations in 304 stainless steel. *J Nucl Mater.* 2011;409(1):18–26.
39. Robach JS, Robertson IM, Wirth BD, Arsenlis A. In-situ transmission electron microscopy observations and molecular dynamics simulations of dislocation-defect interactions in ion-irradiated copper. *Philos Mag.* 2003;83(8):955–67.
40. Suzuki M, Fujimura A, Sato A, Nagakawa J, Yamamoto N, Shiraishi H. In situ deformation of proton-irradiated molybdenum in a high-voltage electron microscope. *Philos Mag A.* 1991;64:395–411.
41. Kacher J, Cui B, Robertson IM. In situ and tomographic characterization of damage and dislocation processes in irradiated metallic alloys by transmission electron microscopy. *J Mater Res.* 2015;30(9):1202–13.
42. Suzuki, M., A. Fujimura, A. Sato, J. Nagakawa, N. Yamamoto, and H. Shiraishi. In situ deformation of proton-irradiated metals. In *New directions and future aspects of HVEM*, October 8, 1990 – October 10, 1990. 1991. Osaka, Japan.
43. Suzuki M, Sato A, Mori T, Nagakawa J, Yamamoto N, Shiraishi H. In situ deformation and unfauling of interstitial loops in proton-irradiated steels. *Philos Mag A.* 1992;65(6):1309–26.
44. Jin H-H, Shin C, Kwon J. Observation of interaction behavior between microstructural defects and dislocation by in situ strain TEM examination. *J Nucl Mater.* 2013;442(1–3, Supplement 1):S851–5.
45. Drouet J, Dupuy L, Onimus F, Momprou F. A direct comparison between in-situ transmission electron microscopy observations and dislocation dynamics simulations of interaction between dislocation and irradiation induced loop in a zirconium alloy. *Scr Mater.* 2016;119:71–5.
46. Matsukawa Y, Osetsyk YN, Stoller RE, Zinkle SJ. The collapse of stacking-fault tetrahedra by interaction with gliding dislocations. *Mater Sci Eng A.* 2005;400:366–9.

47. Robertson IM, Robach JS, Lee HJ, Wirth BD. Dynamic observations and atomistic simulations of dislocation-defect interactions in rapidly quenched copper and gold. *Acta Mater.* 2006;54(6):1679–90.
48. Briceno M, Kacher J, Robertson IM. Dynamics of dislocation interactions with stacking-fault tetrahedra at high temperature. *J Nucl Mater.* 2013;433(1–3):390–6.
49. Dougherty LM, Robertson IM, Vetrano JS. Direct observation of the behavior of grain boundaries during continuous dynamic recrystallization in an Al-4Mg-0.3Sc alloy. *Acta Mater.* 2003;51:4367–78.
50. Clark BG, Robertson IM, Dougherty LM, Ahn DC, Sofronis P. High-temperature dislocation-precipitate interactions in Al alloys: an in situ transmission electron microscopy deformation study. *J Mater Res.* 2005;20:1792–801.
51. Kacher J, Eftink B, Cui B, Robertson IM. Dislocation interactions with grain boundary interactions. *Curr Opin Solid State Mater Sci.* 2014;18:227–43.
52. Shen Z, Wagoner RH, Clark WAT. Dislocation and grain boundary interactions in metals. *Acta Metall.* 1988;36:3231–42.
53. Lee TC, Robertson IM, Birnbaum HK. TEM in situ deformation study of the interaction of lattice dislocations with grain boundaries in metals. *Philos Mag A.* 1990;62(1):131–53.
54. Kacher J, Robertson IM. In situ and tomographic analysis of dislocation/grain boundary interactions in  $\alpha$ -titanium. *Philos Mag.* 2014;94(8):814–29.
55. Kacher J, Robertson IM. Quasi-four-dimensional analysis of dislocation interactions with grain boundaries in 304 stainless steel. *Acta Mater.* 2012;60(19):6657–72.
56. Sangid MD, Ezaz T, Sehitoglu H, Robertson IM. Energy of slip transmission and nucleation at grain boundaries. *Acta Mater.* 2011;59(1):283–96.
57. Cui B, Kacher J, McMurtrey MD, Was GS, Robertson IM. Influence of irradiation damage on slip transfer across grain boundaries. *Acta Mater.* 2014;65:150–60.
58. Cui B, McMurtrey MD, Was GS, Robertson IM. Micromechanistic origin of irradiation-assisted stress corrosion cracking. *Philos Mag.* 2014;94(36):4197–218.
59. Mompiau F, Legros M, Boe A, Coulombier M, Raskin JP, Pardoën T. Inter- and intragranular plasticity mechanisms in ultrafine-grained Al thin films: an in situ TEM study. *Acta Mater.* 2013;61(1):205–16.
60. Mompiau F, Caillard D, Legros M, Mughrabi H. In situ TEM observations of reverse dislocation motion upon unloading in tensile-deformed UFG aluminium. *Acta Mater.* 2012;60(8):3402–14.
61. Wang J, Misra A. An overview of interface-dominated deformation mechanisms in metallic multilayers. *Curr Opin Solid State Mater Sci.* 2011;15(1):20–8.
62. Wang J, Zhou C, Beyerlein IJ, Shao S. Modeling interface-dominated mechanical behavior of nanolayered crystalline composites. *JOM.* 2014;66:102–13.
63. Eftink BP. Dislocation interactions with characteristic interfaces in Ag-Cu eutectic. In: *Materials science and engineering.* University of Illinois at Urbana-Champaign; 2016.
64. Eftink BP, Li A, Szlufarska I, Robertson IM. Interface mediated mechanisms of plastic strain recovery in a AgCu alloy. *Acta Mater.* 2016;117:111–21.